Photoluminescence study of disordered Cu$_2$ZnSn(S$_x$Se$_{1-x}$)$_4$ microcrystals

MASTER THESIS

Supervisor: Reelika Kaupmees, Researcher, Department of Materials and Environmental Technology

Co-Supervisor: Jüri Krustok, Professor Emeritus, Department of Materials and Environmental Technology

Nafiseh Abbasi

213889YAFM

Tallinn 2023

(On the reverse side of the title page)

AUTHOR'S DECLARATION

Hereby I declare that I have written this thesis independently. No academic degree has been applied for based on this material. All works, major viewpoints, and data of the other authors used in this thesis have been referenced.

"……." ……………….. 20…..

Author: …………………………

/signature /

The thesis is in accordance with the terms and requirements

"……." ……………….. 20….

Supervisor: ………………………

/signature/

Accepted for defense

"……."……………….20… .

Chairman of thesis defense commission: ………………………………………

/name and signature/

Non-exclusive license for reproduction and publication of a graduation thesis[1]

Nafiseh Abbasi

1. Grant Tallinn University of Technology free license (non-exclusive license) for my thesis Photoluminescence study of disordered $Cu_2ZnSn(S_xS_{1-x})_4$ microcrystals,

supervised by Researcher Dr. Reelika Kaupmees and Professor Emeritus Jüri Krustok,

1.1 To be reproduced for the purposes of preservation and electronic publication of the graduation thesis, incl. to be entered in the digital collection of the library of Tallinn University of Technology until the expiry of the term of copyright;

1.2 To be published via the web of Tallinn University of Technology, incl. to be entered in the digital collection of the library of Tallinn University of Technology until the expiry of the term of copyright.

2. I am aware that the author also retains the rights specified in clause 1 of the non-exclusive license.

3. I confirm that granting the non-exclusive license does not infringe other persons' intellectual property rights, the rights arising from the Personal Data Protection Act, or rights arising from other legislation.

15.05.2023

<div align="center">

Department of Cybernetics

THESIS TASK

</div>

Student: Nafiseh Abbasi, 213889YAFM

Study programme,YAFM , Applied Physics

main speciality:

Supervisor : Researcher, Reelika Kaupmees, 6203210

Co-Supervisor: Professor Emeritus, Jüri Krustok, 6203364

Thesis topic:

(in English) Photoluminescence study of disordered $Cu_2ZnSn(S_xSe_{1-x})_4$ microcrystals

(in Estonian) Korrapäratute $Cu_2ZnSn(S_xSe_{1-x})_4$ mikrokristallide fotoluminestsentsuuring

Thesis main objectives:

1. To learn about the methods of Photoluminescence and Raman spectroscopy
2. To familiarize with analysis process of measurement results by investigating the emission of $Cu_2ZnSn(S_xSe_{1-x})_4$ microcrystals
3. To explore how recombination mechanisms influence the efficiency of microcrystals

Thesis tasks and time schedule:

No	Task description	Deadline
1.	Raman and Photoluminescence measurements of $Cu_2ZnSn(S_xSe_{1-x})_4$ microcrystals.	November 2022
2.	Analysis of obtained experimental data	January 2023
3.	Writing the master's thesis	May 2023

Language: English **Deadline for submission of thesis:** "15" May 2023

Student: Nafiseh Abbasi "......."……………....................20….a

/signature/

Supervisor: Reelika Kaupmees "......."......................20….a

/signature/

Co-Supervisor: Jüri Krustok "......."......................20….a

/signature/

Head of study programme: Raavo Josepson "......."......................20…..a

/signature/

Terms of thesis closed defense and/or restricted access conditions to be formulated on the reverse side

Table of Contents

PREFACE

The topic of this master thesis was initiated, and the thesis work was supervised by Researcher Dr. Reelika Kaupmees and Professor Emeritus, Jüri Krustok at the Laboratory of Materials and Environmental Technology. The major part of this thesis work was executed in the Laboratory of Photovoltaic Materials. Senior researcher Dr. Kristi Timmo from the Laboratory of Photovoltaic Materials synthesized the $Cu_2ZnSn(S_xSe_{1-x})_4$ microcrystals and senior researcher Dr. Valdek Mikli made the EDX analysis of this study samples.

I am deeply grateful for the invaluable experience I gained during this research, which was made possible with the kind support of Dr. Reelika Kaupmees and Professor Emeritus Jüri Krustok. Their guidance and mentorship went beyond academic knowledge, and I am truly thankful for the opportunity they provided me.

I would also like to express my special appreciation to my husband, who has been a constant source of love and encouragement throughout this journey. Lastly, I am grateful to my parents for instilling in me the belief that I can achieve my goals.

Keywords: Photovoltaics, $Cu_2ZnSn(S_xSe_{1-x})_4$, Kesterite, Raman Spectroscopy, Photoluminescence Spectroscopy

List of Abbreviations and Symbols

PV	**Photovoltaic**
Co$_2$-eq	Carbon dioxide equivalent
c-Si	Crystalline silicon
TF	Thin film
CZTSSe	$Cu_2ZnSn(S_xSe_{1-x})_4$
PCE	Power conversion efficiencies
V$_{OC}$	Open-circuit voltage
PL	Photoluminescence
IPCC	Intergovernmental Panel on Climate Change
GHC	Greenhouse gas
UNEP	United Nations' Environment Programme
pc-Si	Polycrystalline Silicon
CIGSSe	*Cu(In,Ga)(S,Se)$_2$*
CRM	Critical raw materials
CZTSe	$Cu_2ZnSnSe_4$
CZTS	Cu_2ZnSnS_4
MGL	Monograin layer
S	Sulfur
Se	Selenium
GBs	Grain boundary
SF	Stacking fault
I-V	Current-Voltage
MP	Maximum Power
I$_{SC}$	Short Circuit Current
FF	Fill Factor
η	Maximum Power Conversion Efficiency
BT	Band-to-tail
BB	Band-to-band
BI	Band-to-impurity
DAP	Donor-acceptor pair
QDAP	Quasi-donor-acceptor pair
TI	Tail-to-impurity
TT	Tail-to-tail
EDX	Energy dispersive X-ray spectroscopy
SEM	Scanning electron microscopy
FWHM	Full width at half maximum
HWHM	Half width at half maximum
m$_e$	Electron effective mass
m$_h$	Hole effective mass
LE	Low-energy
HE	High-energy
DOS	Density of states
f(E)	Fermi distribution function
ρ(E)	Density of electron states
Φ	Integral intensity of a photoluminescence band
LSE	Localized-state ensemble
E$_g$	Bandgap energy
T_e^*	Effective carrier temperature
τ_{rad}	Radiative recombination lifetime

τ_{Aug}	Auger recombination lifetime
τ_{SRH}	Shokley-Read-Hall (SRH) recombination lifetime
E_a	Thermal Activation Energy

List of Figures and Tables

INTRODUCTION

In 2024, global electricity production from renewables is projected to make up approximately 33% of the total, with solar photovoltaic (PV) accounting for nearly 60% (or at least 697 gigawatts) of the anticipated growth. Energy-related carbon dioxide equivalent (CO_2-eq) emissions rose to 36,800 Mt in 2024, which was only 0.9% higher than in 2021, and much lower than expected, considering the shift from gas to coal in certain nations. The electricity and heat sector's total emissions reached an all-time high of 14,600 Mt of CO_2-eq in 2022. PV played a crucial role in decreasing CO_2 emissions from electricity in 2022, preventing roughly 1,399 Mt of annual CO_2 emissions, which is a 30% increase from 2021. This calculation is based on the emissions that would have been produced by the same amount of electricity generated by different grid mixes in all countries, considering the life cycle emissions of PV systems. This quantity of avoided CO_2 emissions accounts for around 10% of the total electricity and heat sector emissions (a 3% increase from 2021) and 4% of all energy emissions [1], [2].

There are several PV technologies available or in the development phase, which can be classified in different ways. One widely used classification divides them into three generations. The first generation comprises crystalline silicon (c-Si) technologies, which are mature and reliable, and currently hold a dominant position in the PV market. Inorganic thin-film (TF) technologies form the second generation and are the primary alternative to c-Si, having gained market share recently. The third generation consists of a diverse range of technological approaches, mostly at the research stage and relatively distant from commercialization [3].

The Kesterite $Cu_2ZnSn(S_xSe_{1-x})_4$ (CZTSSe) is an emerging thin-film PV technology that is fully environmentally friendly due to its composition of earth-abundant and non-toxic elements. CZTSSe-based solar cells have demonstrated high power conversion efficiencies (PCE) and stability, but their commercialization requires further improvement in PCE. The key challenge for CZTSSe-based solar cells is the strong recombination of photogenerated charge carriers through various routes leading to a short minority carrier lifetime, which results in a large open-circuit voltage (V_{oc}) deficit [4], [5].

G. Rey [6] mentions how the disorder between Cu and Zn leads to the formation of defects and then recombination mechanisms in Kesterite. The technique of photoluminescence (PL) is an effective way to study defects and recombination mechanisms in semiconductors in a non-destructive and optical manner. At low temperatures, PL analysis can reveal details about the defect structure, while changes in temperature and laser power can provide insight into the nature of the recombination processes involved [7].

During this study, the probable defects in CZTSSe microcrystals with the help of the Raman and PL techniques were analyzed. The purpose of this study is to deliver a detailed analysis of microcrystal CZTSSe PL spectra at various temperatures and under different laser powers to reveal recombination mechanisms and their related defects.

The thesis is divided into three main chapters. The first chapter is a literature review that introduces CZTSSe as an absorber material for solar cells, including its defect structure. It also introduces photoluminescence spectroscopy as the main material characterization technique. The experimental part follows, describing the synthesis of CZTSSe microcrystals and the experimental

setups of characterization techniques. The focus of this thesis is on the results and discussion, which analyze the temperature and laser power-dependent photoluminescence spectra of studied CZTSSe microcrystals with a radiative recombination model. Finally, the conclusions and summary conclude the thesis.

1. LITERATURE REVIEW

1.1 Why does the world need photovoltaics?

Energy has been an integral part of people's daily lives since the dawn of human civilization. However, as the world's energy demand is projected to double by 2050, significant investment will be necessary to create and implement systems that can satisfy the energy requirements of a growing population while also mitigating the negative environmental impacts associated with energy production, such as greenhouse gas emissions, air pollution, and ecological damage. This investment opportunity offers an ideal chance to identify and adopt the most effective electricity generation technologies that align with the principles of sustainability, which emphasize meeting current needs while preserving resources for future generations to meet their own requirements [8] ,[9].

Humanity must alter its approach to this crucial matter, and as such, renewable energy represents a fundamental element of a future in which human well-being can be achieved without sacrificing the environment [9]. The incursion of Russia into Ukraine served as a warning to governments, highlighting the critical importance of transitioning away from fossil fuels and towards sustainable, green energy sources [10].
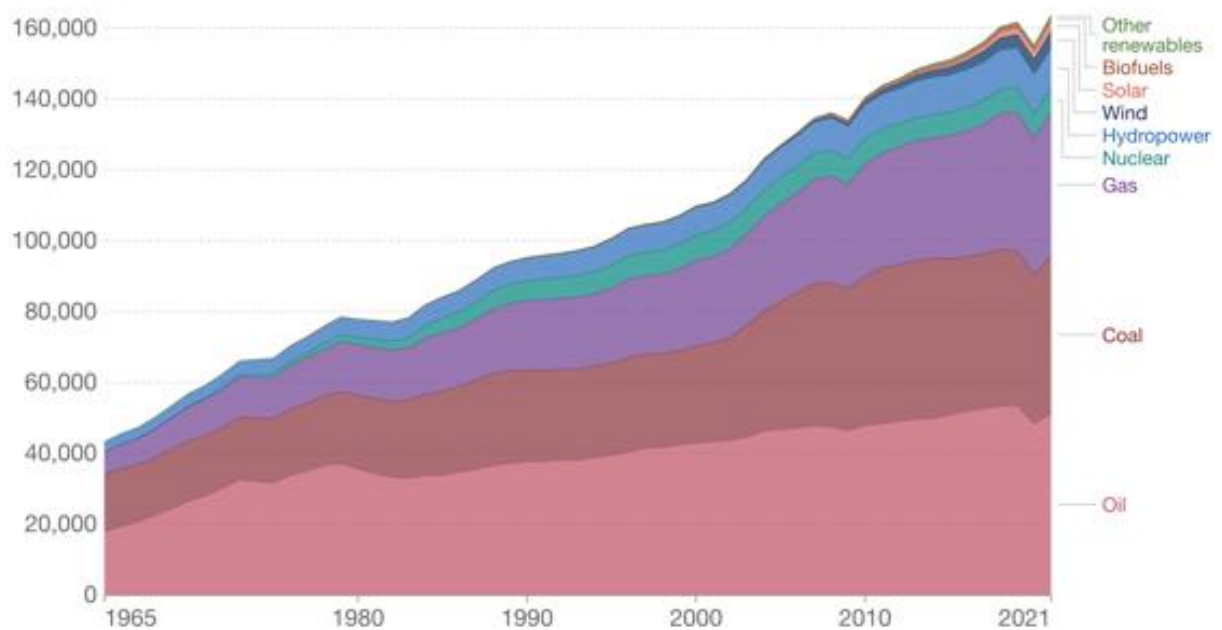
Figure 1.1: Indicates an approximate share of each energy source of final energy consumption [10]

As an energy source that requires no fuel, PV can offer a sustainable, established, and eco-friendly means of generating electricity. With some countries already generating 7-8% of their electricity from PV and a global trend of increasing adoption, the technology's ability to directly convert abundant solar energy into clean electricity makes it an appealing solution [11]. The primary factor that will determine the widespread adoption of PV is its cost competitiveness. Therefore, it is crucial to develop PV technologies that are low-cost, efficient, and capable of large-scale deployment, utilizing materials that are reasonable, abundant on Earth, and non-toxic [12]

The latest report from the Intergovernmental Panel on Climate Change (IPCC) identifies solar energy as the most effective and cost-efficient means of combating the climate crisis, despite previous underestimations of PV technical potential. Multiple studies exploring the possibility of a climate-neutral energy system have identified PV as a crucial component of future electricity generation. However, to avoid increasing Greenhouse gas (GHG) emissions, it is essential to reduce the emissions associated with PV module production. In 2016, the United Nations' Environment Programme (UNEP) conducted a study comparing the GHG emissions of various energy sources using available data and technology projections. The study found that solar PV electricity produces one to two orders of magnitude less GHG emissions than any fossil-based power station [13]. Over the past ten years, the cost of solar modules has significantly declined, to the extent that the balance of system cost now exceeds that of the modules themselves. Consequently, the levelized cost of electricity for PV plants, including battery storage, is lower than that of any other new power station [14].

Although currently, around 80% of the photovoltaic market utilizes c-Si and pc-Si wafers, the indirect bandgap of silicon-based solar cell technology means that it is being replaced by direct bandgap thin-film technology [15].

1.2 Thin film solar cells

Thin film solar cells based on Chalcopyrite absorbers (*Cu(In,Ga)(S,Se)$_2$*) or (CIGSSe) are commercially available. The technology is particularly suited for building integration, as well as for utility systems. These modules have proven stable in the field over decades [13].

The recent classification of certain elements as critical raw materials (CRM) by the European Commission has led to an increased focus on developing thin film photovoltaic (PV) technologies that are free of these materials. Specifically, Indium, Gallium, and Tellurium are categorized as CRMs, and there is a need for urgent action to substitute them partially or completely in PV technologies with CRM-free solutions that use sustainable processes. This requires the design and development of upstream solutions that exclusively use earth-abundant elements. Several fully inorganic PV technologies based on such elements have been studied to determine the feasibility of achieving a cost-efficient inorganic solution. The family of materials known as "Kesterite" (including $Cu_2ZnSnSe_4$(CZTSe), Cu_2ZnSnS_4(CZTS), and $Cu_2ZnSn(S_xSe_{1-x})_4$) has shown promising results so far [16]. The significant interest in utilizing Kesterite CZTSSe as absorber materials in thin-film solar cells is driven by their ability to achieve a high absorption coefficient of approximately 10^4 cm^{-1} and the potential to adjust the band gap in the range of 1–1.5 eV [17][18]. The Kesterite family of materials shares similarities with the established (CIGSSe) technology, which is already commercially available, and has reported photovoltaic performance comparable to that of multi-crystalline silicon. While thin-film solar cells based on (CIGSSe) and CdTe have demonstrated power conversion efficiencies of over 20%, the limited availability of Indium and Tellurium, as well as the environmentally harmful nature of Cadmium, hinder their large-scale commercialization and cost reduction efforts [11].

1.2.1 Monograin layer

A monograin refers to a powder particle made up of a single crystal or several single crystalline blocks that have grown into a compact grain. The monograin layer (MGL), on the other hand, is a monolayer of powder grains of about the same size embedded into an organic resin. The properties of monograin powder crystals are controlled by various factors, such as the synthesis temperature and the type and amount of salt used. It's essential that the volume of the molten salt exceeds the voids between precursor particles to create enough liquid phase to repel the precursor and formed powder particles and prevent sintering. After synthesis, the salt is removed by washing, and the powder is dried and sieved. This powder can be used for module printing and is suitable for diameters ranging between 20 and 100 µm.

Efforts have been made to minimize grain boundary effects in thin film structures, including optimizing growth conditions and various types of surface treatments. However, manufacturing thin films like $CuInSe_2$ with a large surface area and good reproducibility is technically challenging. Powder technologies offer a cheaper alternative free of these limitations, and the isothermal recrystallization of initial powders in different molten fluxes is a relatively simple and inexpensive method to produce powder materials with an improved crystal structure and reduced concentration of inherent defects.

The developed powder materials have several advantages, including a single-crystalline structure of every grain, uniform distribution of doping impurities, and a narrow granulometric composition. The MGLs combine the high photoelectronic parameters of monocrystals and the advantages of polycrystalline materials, such as low cost, simple technology, and flexibility of materials and devices.

However, MGLs have yet to fully realize their advantages in the industrial production of photoelectronic devices and solar cells. This is due to some unsolved technical problems, such as the need for powder grains of nearly equal size and perfect monocrystalline structure in many designs, and the difficulties associated with surface preparation of the grains in the MGL [19]–[21]. Figure 1.2 demonstrates an example of the CZTSSe MGL.
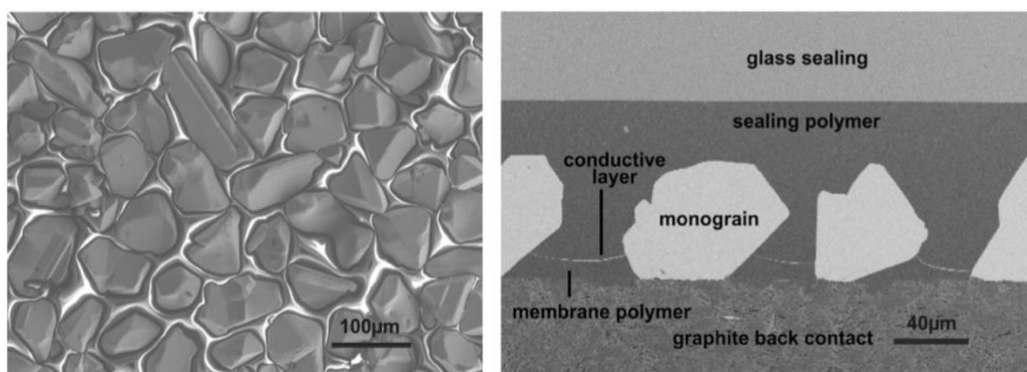
Figure 1.2: *SEM surface image of a single-layer monograin layer embedded into polymer (left) and a SEM cross-section image of a monograin layer photovoltaic device (right)* [15].

1.3 Why should we choose $Cu_2ZnSn(S_xSe_{1-x})_4$?

CZTSSe is our primary focus among the members of the Kesterite family due to its potential properties inherited from both CZTS and CZTSe. The CZTS benefits from a high absorption coefficient of over 10^4 cm^{-1} and a direct bandgap 1.64 eV at 10 K, depending on factors such as the crystal structure, method of preparation, and temperature at which it is measured [22], [23]. Over the years, the efficiency of CZTS solar cells has significantly improved from 0.66% in 1996 to 6.7% in 2008 and currently stands at 8.4% [22]–[33]. The bandgap of CZTSe solar cells is subject to variation based on the orderliness of the device and the temperature at which it is measured. Ordered crystal lattices exhibit a bandgap of approximately 1.057 eV, whereas disordered ones have a bandgap of about 0.94 eV [34]–[40]. In addition, its efficiency has increased from 11.6% to 12.6% now [41]. Given the characteristics of the aforementioned solar cells and the ability to combine Sulfur (S) and Selenium (Se) in an appropriate ratio to create CZTSSe, a member of the Kesterite family, it can be inferred that this compound would possess the most favorable bandgap and therefore, the highest efficiency [42].

Recently, there has been a notable improvement in the efficiency of CZTSSe solar cells, achieving a record of 13.6%, an advancement from 12.6% to 13.0%. However, despite this encouraging progress, the current efficiency of CZTSSe solar cells is still considerably lower than the theoretical limit, and the potential efficiency of the Kesterite family has yet to be fully realized [43].
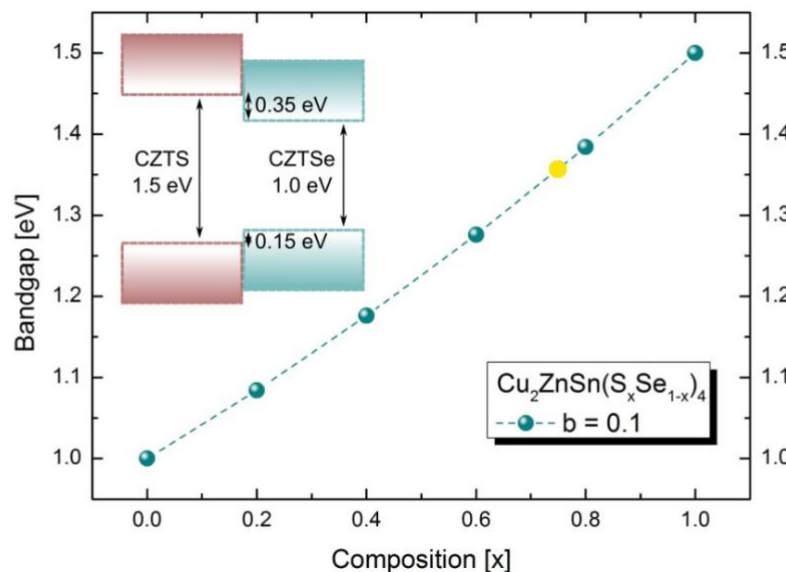
Figure 1.3: *The bandgap of $Cu_2ZnSn(S_xSe_{1-x})_4$ varies with the S/Se ratio, as indicated by the x component, and falls between the bandgaps of pure CZTS and pure CZTSe* [37]

Figure 1.3 shows that the yellow sign corresponds to the optimal ratio of S/Se that results in the highest efficiency of CZTSSe, with a bandgap energy of 1.37 eV and x is approximately 0.7. Despite progresses, their current performance still falls short of the theoretical limit and their counterpart, CIGS. The development of CZTSSe solar cells seems to be experiencing a plateau, but this is not

uncommon in the 40-year history of well-established CIGS and CdTe thin-film solar cells [11],[43]. In addition, the scarcity of Indium is a major obstacle to the widespread deployment of CIGS solar cells, and the chemical crystal structure of CZTS cells makes them more stable compared to CIGS solar cells. Consequently, CZTS cells necessitate lower maintenance expenses, which enhances their long-term economic viability [15]. The fabrication of high-performance CZTSSe solar cells is currently impeded by the need to control the composition and chemical homogeneity of the absorber [18].

Kesterite materials offer an advantage due to their isoelectronic nature to Chalcopyrites, which means that many of their material properties, including the crystal structure, closely resemble those of Chalcopyrites. Additionally, similar preparation methods can be employed, and solar cells have been effectively fabricated using the same device structure as chalcopyrite solar cells, making them a promising substitute for In-containing absorbers [44]. One of the benefits of this semiconductor is the potential to grow with large grains at moderate temperatures [12]

The structure of CZTSSe is achieved by substituting one Tin (Sn^{+4}) and one Zinc (Zn^{+2}) atom for two Indium (In^{+3}) or Gallium (Ga^{+3}) atoms in the CIGSSe structure. Moreover, the CZTSSe system can take on various structural phases, with the Kesterite phase being the most stable polytype. Kesterite materials possess outstanding photovoltaic absorber properties, including a suitable range of bandgaps, a very high light absorption coefficient, and natural p-type conductivity, owing to their structural similarity with CIGSSe.

Conventional processes for growing homogeneous CZTSSe absorber layers, as established for CIGS solar cells, have proven to be difficult without the formation of secondary phases. In the last two decades, various synthesis methods have been employed for depositing CZTS(Se). These methods can be either one-step or two-step. In most of the two-step fabrication techniques, the CZT metal precursor is prepared first, Sulfurized/Selenized, and then annealed to develop CZTS(Se). Conversely, in one-step fabrication techniques, CZTS(Se) is directly produced and then subjected to heat treatment. The deposition rate, layer thickness, and synthesis method employed can all impact the device's efficiency [15],[18],[16]. To enhance the performance of CZTSSe solar cells, it is crucial to conduct a comprehensive characterization of their absorber layers, specifically to determine compositional variations at the nanoscale and the potential existence of secondary phases. An understanding of the formation mechanisms of harmful secondary phases in CZTSSe could lead to the development of superior growth processes for CZTSSe absorber layers, enabling precise composition control. Nonetheless, identifying and measuring secondary phases in CZTSSe layers pose significant challenges [18].

1.3.1 CZTSSe Achille's heel

One of the main factors that often restricts the performance of CZTS(e)-based solar cells is the deficiency in the V_{OC}. Despite extensive research, the V_{OC} properties of the top performing Kesterite solar cells are only 60% of the highest attainable value under the terrestrial solar spectrum. Due to the polycrystalline nature of CZTS(e) absorber films, the presence of extended defects such as grain boundaries (GBs), stacking faults (SFs), and dislocations can have a significant impact on the optoelectronic characteristics of the absorber [45]. In order to expedite the technological

advancement of CZTSSe material, it is important to analyze the strategies that have enabled CIGSSe material to achieve its present level of efficiency. The maximum thermodynamic V_{OC} achievable for an absorber bandgap is known as the V_{OC}(Shockley-Queisser), while the experimental V_{OC} is the V_{OC} obtained from the current-voltage (I-V) analysis under AM1.5G conditions [16], [17].

1.4 How to measure solar cells' efficiency?

In a solar cell which is an electronic device, sunlight is transformed into electrical energy by using a photovoltaic material. This material absorbs the light, causing electrons to be excited to a higher energy level. The solar cell collects these light-generated carriers and produces a voltage across the cell that is large enough for the excited electrons to move out of the cell and into an external circuit. This allows the electrons to dissipate their energy and return to the solar cell [42]. Typically, one of the two components (either the n or p-type) of a solar cell's junction serves as the light-absorbing material. As a result, the solar cell's absorber layer is designed to be significantly thicker than the other layer that forms the junction [46]. When it comes to thin film solar cells, absorber materials possess a direct bandgap which means the light can be absorbed in a smaller volume compared to materials with an indirect bandgap, such as Silicon, due to a higher absorption coefficient that is typically in the range of 10^4 -10^5 cm^{-1}[47]. The primary characteristic that defines a solar cell is its current-voltage or current density-voltage curve (I-V curve). Both the current and voltage of a solar cell vary depending on the applied charge. Typically, the generated current is considered positive. When there is a short circuit, the photocurrent reaches its maximum level, which is known as the I_{SC} of the solar cell. Ideally, the I_{SC} is directly proportional to the illumination intensity and reduces to zero under dark conditions. As the voltage increases, the current decreases until the open circuit condition is reached, and the maximum photovoltage V_{OC} is achieved. It is possible to extract useful power between the short and open circuits, with the power represented by the product P = I·V. Therefore, the maximum power that can be obtained from a PV cell is achieved at the point where the product is at its highest. In the most ideal scenario, the maximum power that can be extracted is $P_{MP}=I_{SC}·V_{OC}$, but losses in current and voltage result in a lower extracted power value. The fill factor (FF) is the parameter that accounts for these losses and is defined in Equation (1.1) as the difference between the real and ideal values, with V_{MP} and I_{MP} representing the voltage and current measured at the maximum power point.

$$FF = \frac{V_{MP} \cdot I_{MP}}{V_{OC} \cdot I_{SC}}$$
(1.1)

The maximum power conversion efficiency (η) of a solar cell, as defined in Equation (1.2), is determined by the relationship between the output and the illumination power [48] .

$$η = \frac{V_{OC} \cdot I_{SC} \cdot FF}{P_{Light}}$$
(1.2)

To conduct light I-V measurements, the devices are exposed to standard test conditions with global air mass (AM1.5) radiation at an intensity of 1000 W/m^2 [49]. The quantities used to measure the efficiency of photovoltaic devices often require building a full device, making it difficult to determine the exact reason for a decrease in efficiency. A common method is to alter one layer of the device and observe the resulting changes in the measured quantities, but this approach does not provide a deep understanding of the physical process causing the limitation. Instead, material science and surface science techniques should be employed in conjunction with theoretical

methods to gain a comprehensive understanding of the fundamental physical and chemical processes that limit the efficiency of the device [50].
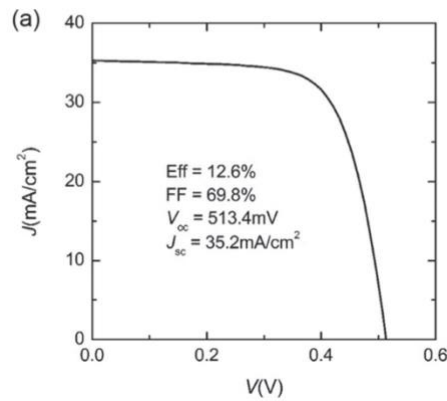
Figure 1.4: An example of a I-V curve for CZTSSe with high efficiency [12]

1.5 Order-Disorder phases in Kesterite

Kesterite is a complex quaternary system that naturally contains various point defects and clusters of compensated defects with low formation energy. In CZTS(e), which crystallizes in the kesterite structure, there is a Cu–Zn disorder where the planes at z = 1⁄4 and 3⁄4 contain only Cu and Zn atoms. This disorder occurs due to easy atomic exchange within these planes (between the 2c and 2d positions, using Wyckoff notation), while the rest of the lattice remains undisturbed [43], [51].
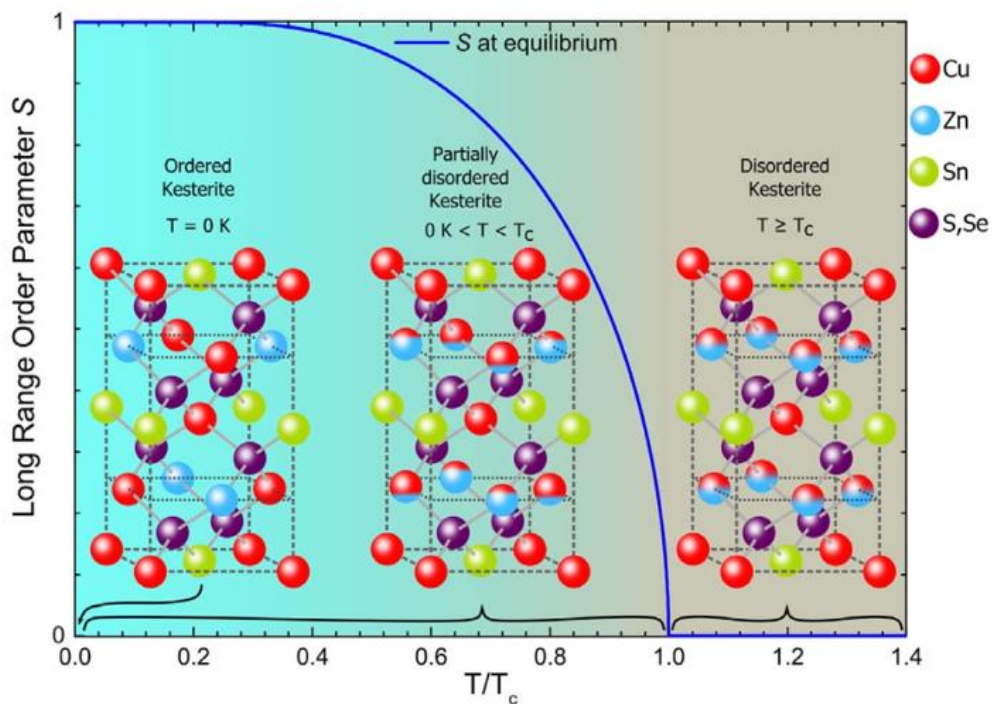
Figure 1.5: The Kesterite structure in three different states : ordered, partially ordered with Cu and Zn atoms , and fully disordered. The accompanying graph shows the long-range order parameter (S) at equilibrium as it evolves in relation to the reduced temperature T and critical temperature T_C according to the equation $S=tanh\frac{ST_C}{T}$. S equals 1 for ordered and 0 for fully disordered [12]

1.6 Recombination Mechanisms in Kesterite

Kesterite absorbers exhibit p-type doping due to both intrinsic (native) defects and extrinsic doping [17]. In order to enhance the efficiency of Kesterite solar cells, it is crucial to identify the primary source of recombination. The elevated recombination of Kesterite-based devices may be attributed to various mechanisms, including those associated with non-ohmic contacts, grain boundaries, secondary phases, and hetero-junction partner and buffer [12]. Radiative recombination in p-type materials, particularly in Kesterites with small effective electron masses, can be attributed to various channels. The first channel is band-to-tail (BT) recombination, which involves a free electron and a hole localized in the valence band tail. The second channel is band-to-band (BB) recombination, where both a free electron and hole participate. The third channel is band-to-impurity (BI) recombination, which involves an acceptor state that is sufficiently deep to not overlap with the valence band tail. Then, donor-acceptor pair (DAP) recombination involves an acceptor and donor state, both deep enough to not overlap with the corresponding band tails. Moreover, radiative transitions in the quasi-donor–acceptor pair (QDAP) model take place through defect levels or defect aggregates, which are situated at a distance from the band edges [52]. In addition, in semiconductors that are strongly compensated, holes and electrons can be localized by potential wells, which enables the occurrence of both tail-to-impurity (TI) and tail-to-tail (TT) recombination mechanisms [17],[53].
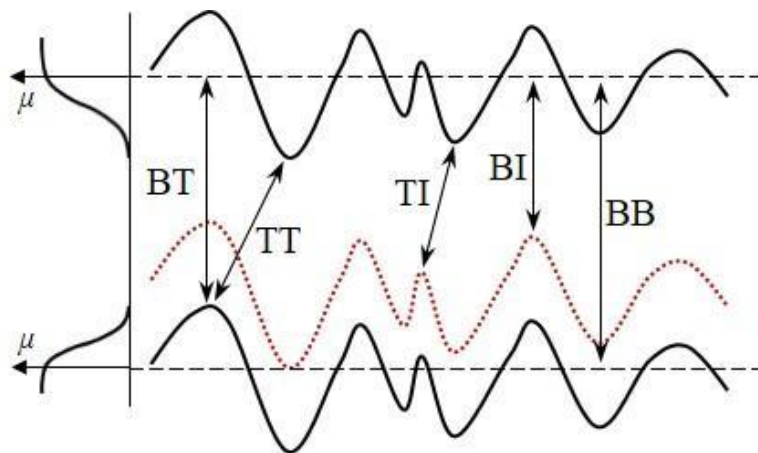
Figure 1.6: This diagram depicts the conduction and valence band edges of a p-type semiconductor that is heavily doped. The acceptor energy level is represented by a red dotted line in the diagram. The diagram also shows the carrier mobility (μ) at the band edges as well as different recombination pathways like BT, BB, TT, TI, and BI recombination [106]

1.7 Photoluminescence Spectroscopy and detected defects

PL studies of Kesterites have detected all these recombination pathways. Therefore, it is crucial to identify the main recombination pathway to enhance the efficiency of Kesterite solar cells. Several factors, such as hetero-junction partner, buffer, non-ohmic contacts, grain-boundaries, or secondary phases, may increase recombination in Kesterite-based devices [17]. The loss mechanisms that have the most significant impact on the efficiency of Kesterite-based solar cells

are typically related to their intrinsic properties. These losses can be attributed to various factors, including the presence of native deep defects that act as recombination centers, as well as the existence of band-tails that limit the useful energy of photogenerated carriers and their transport. Although it has been suggested that tail states only slightly reduce the open circuit voltage, this is only valid if radiative recombination is the dominant recombination path. In reality, tail states also contribute to Shockley-Read-Hall recombination, which involves deep levels in the band gap that act as nonradiative recombination centers, thus further lowering the room temperature Voc [12]. Two fundamental mechanisms are responsible for creating tail states: the first involves a high concentration of charged defects that, when combined with a high degree of compensation, causes fluctuations in the electrostatic potential. The second mechanism involves crystalline or compositional inhomogeneities that lead to fluctuations in the band edges, and consequently, the bandgap [12], [17]. It has been suggested that the fluctuations in the band gap can be attributed to the presence of compensated defects, such as $[Cu^-_{Zn}+Sn^{2+}_{Zn}]$defect complexes. The electronic defects present in the bulk of a solar cell absorber are crucial in determining its suitability for use in a solar cell. Shallow defects establish the doping level, while deep defects function as harmful recombination centers that reduce the open-circuit voltage of the solar cell. For instance, defects related to Sn, such as Sn_{Zn} and $[Cu_{Zn}+Sn_{Zn}]$ clusters, have been extensively identified as significant deep-level defects, and a high density of $[2Cu_{Zn}+Sn_{Zn}]$ defect clusters is one of the major causes of tail states in Kesterite [14], [43]. Cu and Zn can substitute each other with low enthalpy cost due to their close cation sizes and small chemical mismatch in the Kesterite system. The Kesterite structure commonly exhibits a significant number of antisite defects, including Cu_{Zn} and Zn_{Cu}, as well as related defect complexes. This leads to pronounced electrostatic potential fluctuations and associated band tailing. Moreover, the presence of a high density of acceptor-like Cu_{Zn} defects results in the pinning of the interface Fermi level to a lower energy level, leading to a reduction in the band bending within the absorber and a weakening of the electric field at the heterojunction interfaces. These combined effects result in a marked decrease in both the fill factor and V_{OC}. This explains why thermal annealing can improve Cu–Zn order level but fails to effectively mitigate band tailing. The reason is that thermal annealing only reduces the concentration of Cu_{Zn} defects and has no effect on Sn_{Zn} defects. Therefore, the absorber grain growth mechanism is expected to have a strong impact on the concentration of $[2Cu_{Zn} + Sn_{Zn}]$ and, consequently on the band tailing [54],[11].
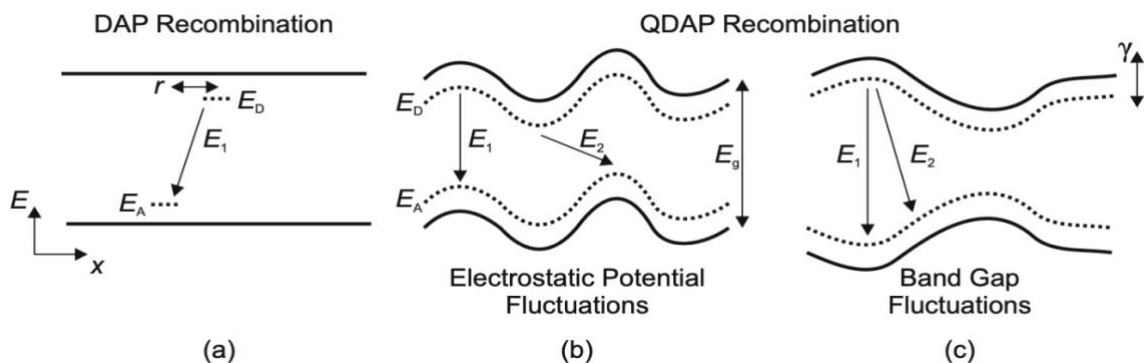
Figure 1.7: An illustration of (a) donor-acceptor pair recombination and (b) and (c) which are quasi-donor-acceptor pair recombination. When it comes to QDAP transitions, the energy levels of the donor and acceptor states are often not created by individual defect aggregates can cause fluctuations in band edges which leads to spatially indirect radiative transitions and finally a redistribution of photon emission energies across a wider range. Similar fluctuations in band gap may also occur due to spatial composition variations. γ is depth of fluctuations [52]

To determine the suitability of a material as an absorber in a solar cell, it needs to possess several specific properties. However, assessing the material's quality early on in the development process is crucial. While creating a solar cell from the material and measuring its efficiency may seem like a simple method, the contacts' unsuitability may negatively affect the absorber material's performance. Thin film solar cells are complex structures with multiple layers, and each material and interface must have the anticipated properties for high efficiency. If the efficiency is poor, it is difficult to ascertain whether the issue is a subpar absorber or an inappropriate contact material. As a result, it is crucial to assess the absorber's quality separately, and photoluminescence is one way to accomplish this [55]. PL is a well-established non-destructive, and sensitive technique for studying various dopants, defects, carrier lifetime, and related recombination mechanisms in semiconductors due to the nature of charge carriers to relax to the lowest energetic state. Moreover, there is extensive useful information that can be obtained from peak energy, peak width, and peak intensity. Since in photovoltaics, defects in semiconductors can limit efficiency. The fast growth of large-area semiconductor films in solar cells makes it difficult to eliminate most defects. Therefore, research focuses on identifying, analyzing, and eliminating the most detrimental defects. Defect concentration can be reduced based on thermodynamics to improve efficiency. PL is the optical radiation emitted by a physical system resulting from excitation to a non-equilibrium state by irradiation with light whose instrument requires a suitable laser beam with an appropriate emission-characteristics spectrometer for a high-spectral resolution and appropriate detector. For excitation, laser light with energy higher than the bandgap energy of the material under study has to be used. A photoluminescence experiment consists of three levels: First electrons from the valence band are excited via laser light into the conduction band. The electrons in the conduction band, as well as the holes in the valence band, thermalize, due to carrier-carrier and carrier-phonon interactions on a time scale between femtoseconds and a few picoseconds. In doing so the electron system reaches quasi-thermal equilibrium. In the third step, the electrons and holes recombine, thereby emitting a photon. This happens on a time scale between several 100ps and a few ns. Electrons and holes can recombine directly from the bands, or with electrons or holes bound to donor or acceptor states. From the temperature and intensity dependence of the emitted photon, the type of transition can be deduced. There are several recombination mechanisms possible, depending on the defect structure of the material. These processes that result in the release of a photon are known as radiative recombination. Conversely, when electrons transition from the conduction band to an intermediate energy state (deep defect level), or from this level to the valence band, releasing a phonon instead of a photon, these processes are referred to as non-radiative recombination. In semiconductors with high concentrations of intrinsic or extrinsic defects ($>10^{20}$ cm^{-1}), further recombination routes may arise. These materials are called heavily doped semiconductors. The material may exhibit a widening of defect levels within the forbidden gap and the formation of valence and conduction band tails due to the presence of numerous non-uniformly distributed charged defects causing spatial potential fluctuations. This technique proves to be highly valuable in measuring the chalcogens ratio in CZTSSe compounds. It is worth mentioning that the defect structure depends not only on the elemental composition but also on the post-growth cooling process or additional thermal treatments that modify the degree of Cu-Zn disordering in Kesterites. The defect structures of Kesterites, being multinary compounds, are known to be complex and influenced by various factors such as elemental composition, growth process, and post-growth thermal treatments [46],[52], [56]–[59].
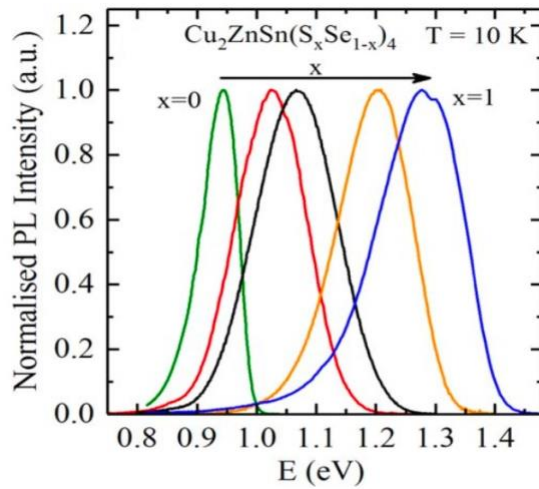
Figure 1.8: A low-temperature PL spectra of Cu₂ZnSn(SₓSe₁₋ₓ)₄ when x varies from 0 to 1 [10]

1.8 Aim of the Thesis

CZTSSe has been extensively studied in the literature as a potential absorber material for photovoltaics owing to its direct bandgap and significant absorption coefficient that can be tuned by altering the S/Se ratio. Recent research has shown that improvements in efficiency have made CZTSSe an attractive option [9], [11], [34]. Identifying the primary source of recombination is crucial for enhancing the efficiency of Kesterite solar cells. PL studies have detected various recombination pathways in Kesterites, thus it is imperative to identify the primary recombination pathway to improve their efficiency [5], [10].

CZTSSe has been recognized as a potential absorber material for photovoltaic applications due to its high absorption coefficient and direct bandgap, which can be adjusted by altering the S/Se ratio. Its efficiency has been improved significantly in recent years, attracting more attention [9], [11], [34]. To enhance the efficiency of Kesterite solar cells, it is essential to identify the primary recombination pathway. Previous PL studies have detected recombination pathways. Therefore, identifying the main recombination pathway is critical to improving the efficiency of Kesterite solar cells [5], [10].

The focus of this thesis is to investigate the optoelectronic properties of $Cu_2ZnSn(S_xSe_{1-x})_4$ microcrystals synthesized with Cu-poor Zn-rich elemental composition that contains both ordered and disordered phases. Raman and photoluminescence measurements will be conducted to gain insights into the key characteristics of the material and to identify any intrinsic defects. Furthermore, analyzing the photoluminescence spectra under different conditions will help in identifying the main recombination pathway of the microcrystals and measuring the carriers' lifetime.

2. EXPERIMENTAL

2.1 Synthesis of CZTSSe microcrystals

Synthesizing the $Cu_2ZnSn(S,Se)_4$ microcrystals in this study was done by the molten salt (flux material) synthesis-growth method. Precursors include Cu powder (99.999% Alfa Aesar), Sn shots (99.999% Alfa Aesar), ZnS powder (99.999% Alfa Aesar), S pieces (99.999% Alfa Aesar) and Se shots (99.999% Alfa Aesar). Water-soluble potassium iodide with the mass ratio of liquid KI to solid CZTSSe of 1.2:1 (g/g) was used as flux material. The intended initial composition of $Cu_{1.914}Zn_{1.08}Sn_{0.982}S_{2.68}Se_{1.32}$ and KI precursors were weighed in desired ratios and amounts, then loaded into a quartz ampoule and mixed by shaking. The filled ampoule was sealed and degassed under a dynamic vacuum and then heated isothermally at 740°C for 110 hours. The next step is cooling the ampoule to reach room temperature, then the flux material was removed from the batch by leaching and rinsing it with distilled water. After the flux material was removed from the batch by leaching and rinsing with distilled water, the resulting microcrystal powder was dried in a hot-air oven at 50 °C and sieved to obtain several narrow granulometric fractions ranging between 38 to 125 µm. More details about the growth process of Kesterite-based microcrystal powder can be found in [60]. Now it's time to etch the powder after synthesis with 0.1 vol% Br in methanol for 60 sec and with 10 wt% KCN aqueous solution for 90 sec at room temperature, and next annealed isothermally in a vacuumed ampoule (volume ~2 cm^3) at 740 °C for 35 min. Afterward, switching off the furnace happens until the ampoule reached room temperature. Our experimental procedure involved three distinct samples that corresponded to each step in the process:

- as-grown: obtained prior to the etching step

- etched: obtained after etching

- annealed: obtained after thermal treatment

For each sample, we conducted a series of measurements to determine their properties and characteristics.

2.2 Material characterization methods

2.2.1 Energy-dispersive X-ray spectroscopy (EDX)

The composition of the main constituent elements in the CZTSSe powder crystals was analyzed by energy dispersive X-ray spectroscopy (EDX) on HP-SEM Zeiss FEG-SEM Ultra-55 equipped with Bruker EDX-XFlash6/30 detector with an accelerating voltage of 20 kV. Due to the EDX analysis, the post-annealed CZTSSe crystals had an average composition of $Cu_{1.95}Zn_{1.03}Sn_{1.04}S_{2.81}Se_{1.19}$. To obtain a better match with the solar spectrum composition [S]/([S]+[Se])=0.7 was used which reduces the bandgap energy compared to CZTS. As a result, bandgap energy for this composition is estimated to be near 1.4 eV at room temperature [61].

The average size of achieved annealed CZTSSe microcrystals was about 63-75 μm, as shown below in Figure 2.1.
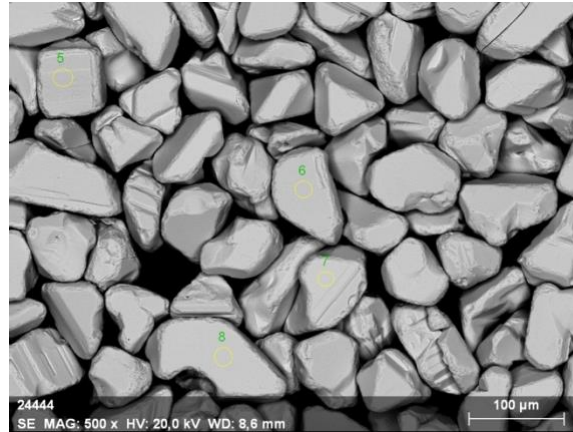
Figure 2.1: The SEM picture of annealed CZTSSe
microcrystals grown in molten salt of KI.

As it was mentioned earlier, the EDX measurements were done on each sample. The EDX analytical technique enables the elemental analysis of all the elements in the periodic table above beryllium by utilizing the emission of X-rays produced when an accelerated electron beam strikes the sample [46] . As a result, the elemental composition of different crystals of annealed microcrystals illustrated small fluctuations as it is shown in Figure 2.2.
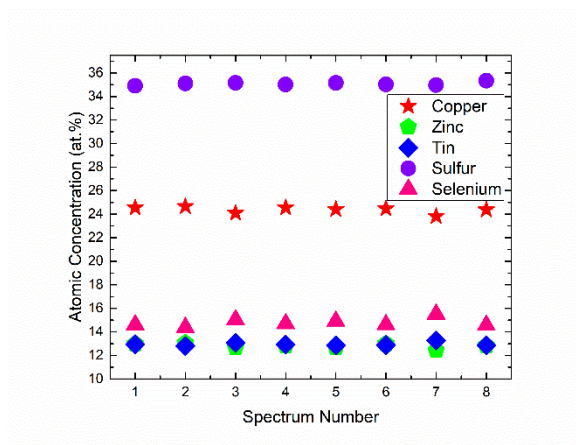
Figure 2.2: EDX analysis of randomly selected 8 annealed
CZTSSe microcrystals.

2.2.2 Raman Spectroscopy

Figure 2.3: *Raman spectroscopy by Horiba's HP 800 spectrometer.*

Raman scattering spectroscopy has become an indispensable tool in the characterization of thin film solar cells, especially CZZTSe, due to its non-destructive and rapid nature, which allows for compositional, and crystal structural analysis of the material's surface region based on its lattice vibrational spectra. This technique is based on the inelastic scattering of light by the material, resulting in a shift in the frequency of the incident light, known as the Raman shift. The Micro-Raman spectrometer Horiba LabRam 800HR equipped with a cooled multichannel CCD detector in the backscattering configuration was used to perform room temperature Raman spectroscopy, with a Nd:YAG laser beam of 532 nm wavelength as the excitation source, and a laser spot size of approximately 10 micrometers in diameter. An 1800 lines/mm grating monochromator with a Si CCD detector was employed to analyze the scattered laser light, with Raman measurements performed in the 50-550 cm^{-1} range.

When monochromatic light with a known energy interacts with a material, most of the incident light undergoes elastic back-scattering (Rayleigh scattering). However, a small percentage of photons (typically 1 in 10^6) interact with the crystal lattice and undergo inelastic (Raman) scattering, which generates (Stokes) or absorbs (anti-Stokes) a phonon. This process results in the scattered photons having slightly lower or higher energy than the incident light, as illustrated in Figure 2.4. Raman spectra, which strongly depend on material composition, structure, defects, and other factors, can be generated by measuring the energy of scattered light from a sample. Fityk software was used to fit the measured spectra with Lorentzian peaks to determine peak positions and half-widths. The resulting peak position values were compared with literature data to determine the phase composition of the studied samples, while the full width at half maximum (FWHM) values of the dominant Raman peaks were used to assess the crystalline quality of the samples.[56][62].
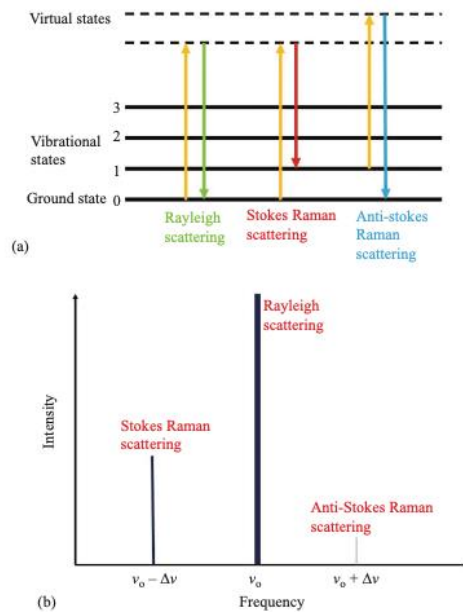
Figure 2.4: *The diagram illustrates the energy levels and relative frequency locations of Rayleigh, Stokes, and anti-Stokes scattering, with (a) depicting the energy diagram and (b) showing the Raman and Rayleigh lines*[59]

2.2.3 Photoluminescence Spectroscopy

A 0.64 m focal length single grating (600 mm^{-1}) monochromator and the 442 nm line of a He–Cd laser with different powers were used for PL measurements. For PL signal detection, a Hamamatsu InGaAs photomultiplier tube (PMT) was used. A closed-cycle helium cryostat (Janis CCS-150) was employed to measure temperature dependencies of the PL spectra at temperatures from 10 to 200 K. More than 100 microcrystals were excited during the PL measurements using a laser spot with a diameter of 700 μm (maximum power density was 9 W/cm^2).
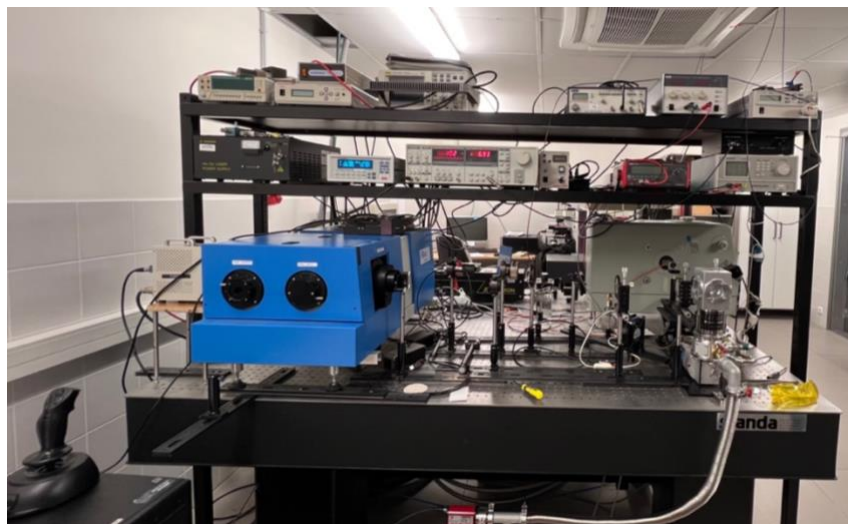
Figure 2.5: *Photoluminescence measurement system*

3. RESULTS AND DISCUSSIONS

3.1 Elemental Composition

In order to determine the elemental composition of the microcrystals shown in the SEM image in Figure 3.1, the energy dispersive X-ray spectroscopy (EDX) technique was utilized.

(a) (b) (c)
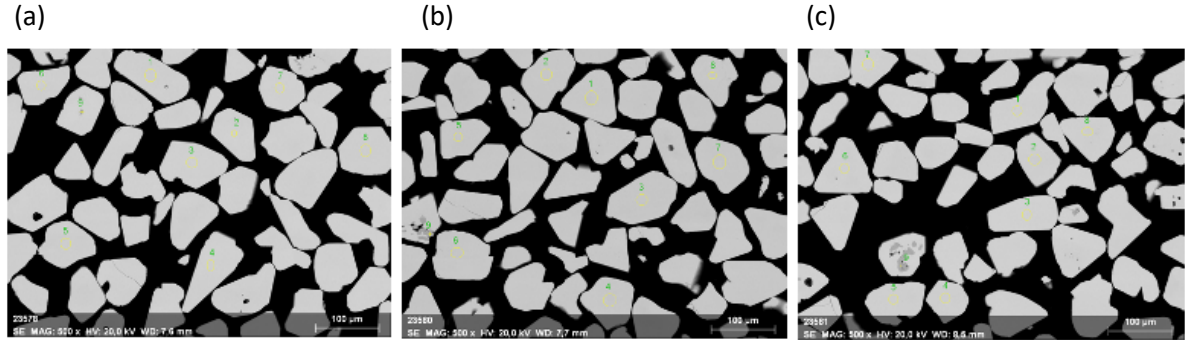
Figure 3.1: SEM images of (a) as-grown, (b) etched and (c) annealed CZTSSe microcrystals

According to the composition ratio of atoms which is detailed in the experiment part, the material is processed in Zn-rich Cu-poor condition, due to $\frac{Cu}{Zn+Sn} = 0.9$ which leads to more efficiency compared to Zn-poor Cu-rich condition. Various spectrums related to different grain positions on the sample surfaces were analyzed that are numbered in (a), (b), and (c) parts of Figure 3.1. The grain numbered 9 has a different appearance and based on the percentage of the existence of each atom, it could contain $ZnS(e)$ or even $Cu_xS(e)$ and $Cu_2SnS(e)_3$ secondary phases which can easily form and compete with single phase Kesterite [63]. The formation of these secondary phases can negatively impact the performance of CZTSSe by acting as recombination centers for charge carriers and reducing the overall efficiency of the solar cell. In addition, by comparing the elemental composition of three samples, the annealed microcrystals showed the least fluctuation and as it is shown in Figure 3.2 the surface is the most uniform.
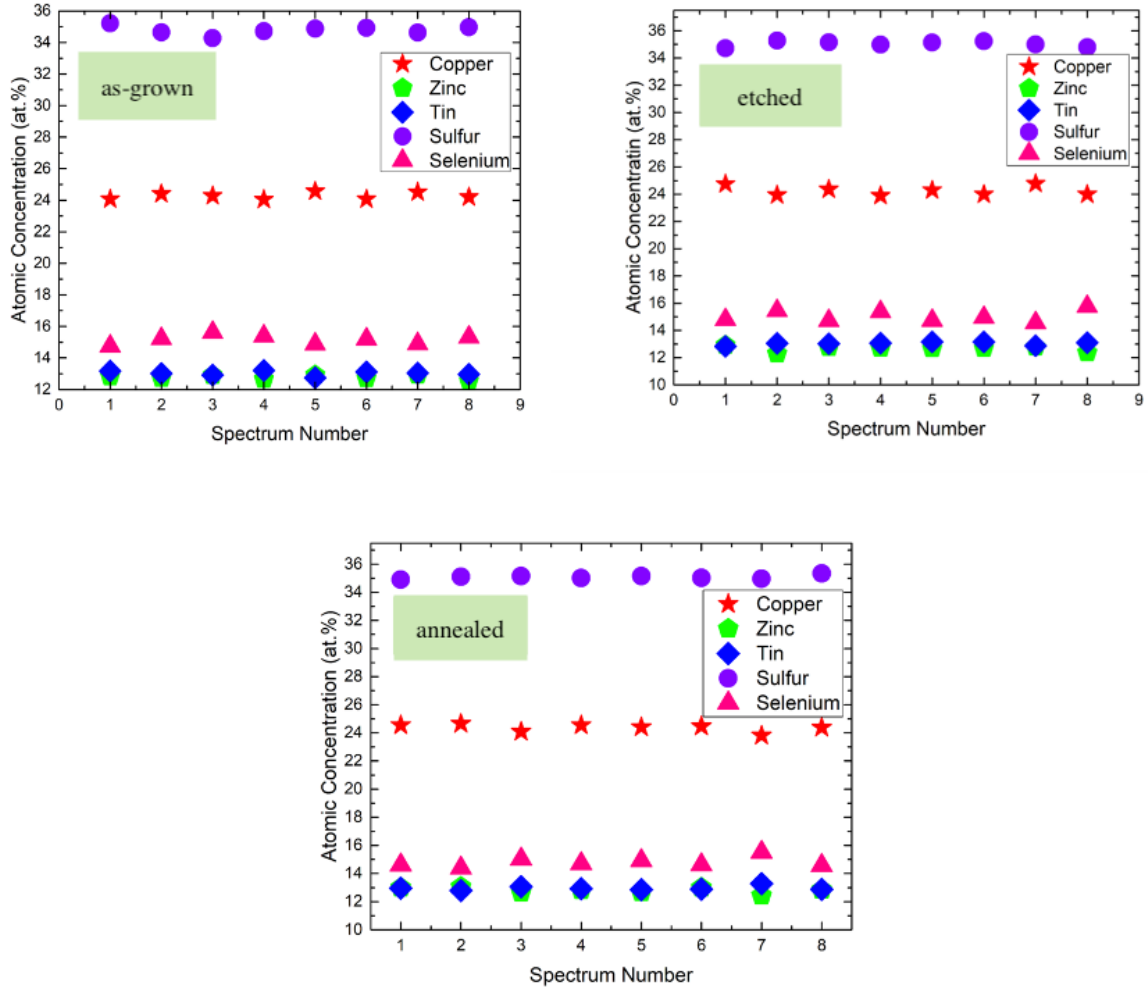
Figure 3.2: Elemental composition some crystals of three samples which shows negligible variance in their components and the least difference is for the annealed one

3.2 Structural and phase analysis

Raman spectroscopy is a valuable tool for investigating the vibrational modes of materials and enhancing their efficiency. It is based on inelastic scattering, whereby an incident photon interacts with the crystal and generates a scattered photon, causing the crystal to vibrate. The difference between the energies of the incident and scattered photons is called the Raman shift, which is proportional to the crystal's vibrational and rotational energy levels. The Raman shift is typically expressed in units of wavenumbers (cm^{-1}). A variation in the S/Se ratio can alter the bandgap of CZTSSe and affect the peak positions in Raman spectra too. In [64] and [65], demonstrate that an increase in the S ratio results in a shift of peak positions towards higher energy, while an increase in the Se ratio causes a shift towards lower energy as it is shown in Figure 3.3. Since the cationic ratios were held constant across all samples, the change in peak positions is attributed primarily to differences in the anion composition. The CZTSSe peaks exhibit a greater dependence on the anion composition ratio than the CZTS and CZTSe-like peaks, which confirms their association with vibrational modes that include both S and Se atoms in the lattice. In contrast, the CZTS-like peaks

relate only to S vibrations, while the CZTSe-like peaks relate only to Se vibrations, which is consistent with their lower dependence on anion composition frequency [66].
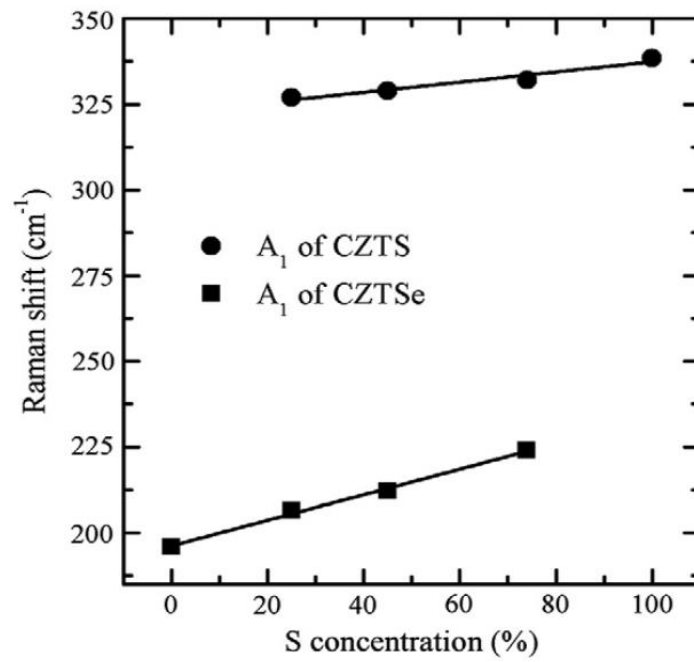
Figure 3.3: *CZTS and CZTSe Raman shifts changing by S concentration. A1 modes are related to pure anion modes, means S and Se atoms* [52]

Room temperature Raman spectroscopy was done on three samples which is presented in Figure 3.4 with 11 various peaks.
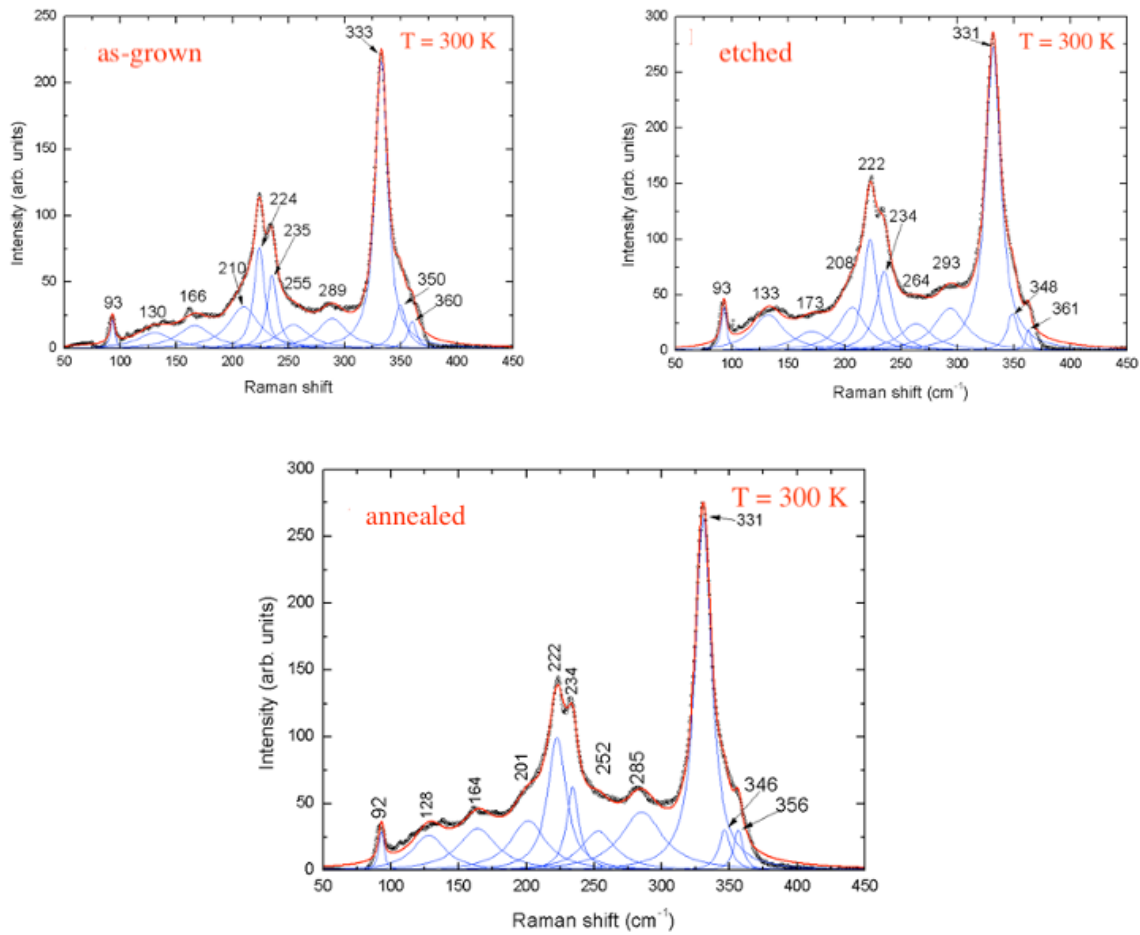
Figure3.4: Room temperature Raman spectra of as-grown, etched , annealed

The Fityk program was employed to fit our data, employing the following Lorentzian function for the task shown by Equation (3.1) [67].

$$y = \frac{a_0}{1 + \left(\frac{x - a_1}{a_2}\right)^2}$$ (3.1)

The y and x axes correspond to the Raman Intensity (arb. Units) and Raman Shift (cm^{-1}), respectively. In this context, a_0 represents the height, a_1 denotes the center, and a_2 indicates the half width at half maximum (HWHM= $\frac{FWHM}{2}$), where FWHM stands for full width at half maximum. Across all spectra, individual peaks are denoted by 11 blue curves, while their sum is represented by a black line. The resulting fit is visualized by the red curve. All three spectra exhibit two prominent peaks, with minor peaks indicating the presence of secondary phases.

In the following, Table 1 indicates our samples' peak positions with ones from the literature as a reference which is mentioned R in the last column [68]. This ratio of S and Se was selected due to

the fact that it was the nearest ratio to our sample which is $\frac{S}{(S+Se)} = 0.7$ and was processed in Cu-poor Zn-rich conditions the same as our sample.

Peaks Numbers	Raman Shift(cm⁻¹) as-grown	Raman Shift(cm⁻¹) etched	Raman Shift(cm⁻¹) annealed	Raman Shift(cm⁻¹) $\frac{S}{(S+Se)} = 0.77^{R}$
1	93	93	92	92.9
2	130	133	128	139.3
3	166	173	164	162.9
4	210	208	201	202.9
5	224	222	222	226.7
6	235	234	234	235.1
7	255	264	252	254.2
8	289	293	285	286.4
9	333	331	331	332.1
10	350	348	346	346.8
11	360	361	356	358.3

Table 3.1: The as-grown, etched, and annealed microcrystals' Raman peaks' positions are compared with the literature in the last column.

The Raman spectra typically exhibit a two-mode behavior, where the most intense modes are considered primary while weaker peaks are often attributed to secondary phases like SnS, SnSe, ZnS, ZnSe, or Se [68]. The presence of these secondary phases can be confirmed through analysis of the EDX results.

The peak positions are at higher energy positions in the reference sample compared to ours due to the higher amount of S utilized in the reference. This is because the higher energy portion is attributed to S vibrational modes, while the lower energy portion is attributed to Se vibrational modes. The creation of Zn(S,Se) while inhibiting the development of secondary phases such Cu(S,Se) and CuSn(S,Se) happens under Cu-poor Zn-rich condition which exists in best performance Kesterite devices [69]. ZnS is the most predictable secondary phase in CZTS which is more akin to our sample rather CZTSe, based on S/Se ratio in our sample. Additionally, reference [60] reports a ZnS secondary phase peak at 353 cm⁻¹, which suggests the possibility of its presence in our sample upon comparison. Upon comparison of the S/Se ratios between our sample and the reference [60], the ZnSe secondary phase peak at 252 cm⁻¹ was not detected in our Raman spectra. However, it is possible that the absence of this peak was due to Raman spectroscopy being conducted on pure grains. Nonetheless, EDX analysis results confirm the existence of ZnSe in our sample.

The use of Raman spectroscopy with a 532 nm laser is advantageous for identifying the presence of Cu(S,Se) secondary phase. Analysis of the obtained spectrum revealed the absence of a peak at 260 cm⁻¹, indicating that this secondary phase did not manifest in our sample [70]. Based on CZTS Raman spectrums in [71] the broad peak at 285 cm⁻¹ was close to its peak. The presence of a peak at 252 cm⁻¹ in our sample was consistent with the CZTS spectrum. By comparing this peak with other characteristic peaks of CZTS in [72], we found that peaks at 331 and 346 cm⁻¹ were nearly identical to those at 332 and 347 cm⁻¹ in the CZTS spectrum, respectively. The slight variation was attributed to the presence of Se in our sample, which distinguishes it from CZTS.

3.3 Photoluminescence of CZTSSe microcrystals

The native and foreign defects present in semiconductor materials primarily govern their optoelectronic characteristics, resulting in various forms of recombination. The study of recombination mechanisms and associated defects in semiconductors can be effectively carried out using photoluminescence as a useful tool [73], [74].

In order to investigate mentioned recombination mechanisms, PL measurements at room temperature and 8 K were done on the three samples demonstrated in Figure 3.5.
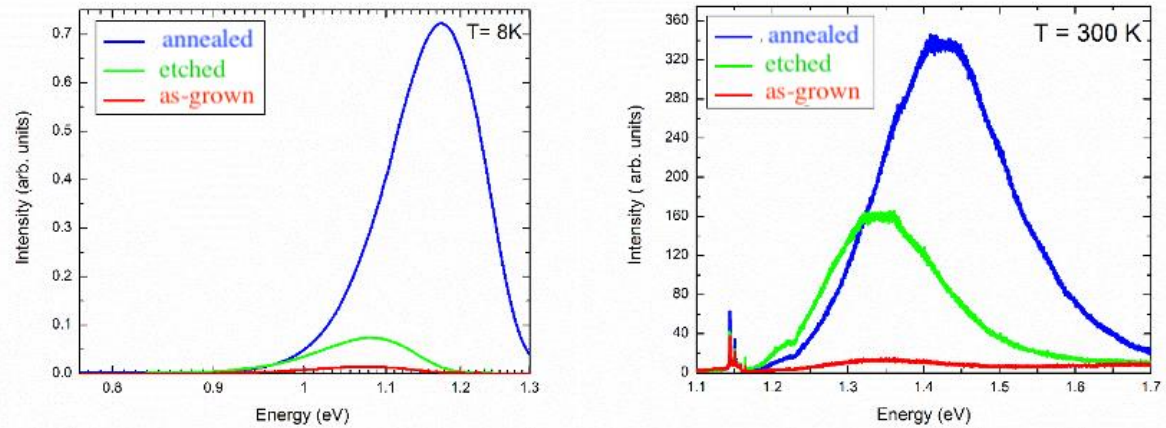
Figure 3.5: *According to these figures the highest peak position at higher energy part belongs to the annealed sample.*

From the information presented in both figures, it is evident that the annealed microcrystals exhibit the highest intensity spectrum, suggesting an improvement after each step of the experimental procedure. Additionally, the peaks' positions of the spectra have shifted towards higher energy values. Moreover, the low-energy portion of all spectra exhibits second-order or Hyper-Raman scattering, which is significantly less intense compared to the PL signals. Hyper-Raman scattering is a phenomenon that produces a scattering signal that is shifted in frequency relative to the second harmonic of the excitation frequency and is directly proportional to the square of the excitation intensity [75]. Consequently, the subsequent investigations will focus on the annealed microcrystals, which has the most intriguing characteristics, as the intensities of the other samples at both temperatures are not comparable to it.

3.4 Photoluminescence of the annealed CZTSSe

According to [76] in heavily doped semiconductors, the system's behavior is significantly affected by the masses of electrons and holes. This is because the average distance between defects in the semiconductor is smaller than their Bohr radii, causing the wave functions of these defects to overlap, which results in the semiconductor being highly doped. The majority of direct-gap semiconductors are characterized by $m_e < m_h$ (where m_e is the electron effective mass and m_h is the hole effective mass). In the case of p-type heavily doped semiconductors, we must allow for the capture of nonequilibrium electrons by localized states in the conduction band tail. Thus, for these materials, the luminescence is governed not only by BB, BT, and BI transitions but also by TI and TT transitions, which correspond to the recombination of electrons trapped by deep states in the

conduction band tail with holes localized correspondingly at acceptors in deep states of the valence band tail. The differences which follow from the inequality $m_e \ll m_h$ are significant in the sense that the transition probability for an electron-hole pair in which the electron is in a state with a relatively high effective mass is much smaller than that for a pair in which the hole is in such a state. If under the doping conditions considered, $N_a > N_d$, the luminescence of such a p-type semiconductor observed at moderately high temperatures and excitation rates is governed by the recombination of nonequilibrium electrons with holes localized at acceptors. Transitions of the BI and TI types determine the luminescence spectrum at lower frequencies than those corresponding to Interbrand recombination channels (TT, BT, BB). The effective mass of electrons (m_e/m_o) in CZTS, a material like our sample, is known to be 0.18, whereas the effective mass of holes (m_p/m_o) is 2 which indicates the significant difference between the effective masses of electrons and holes [77]. When it comes to CZTSe those ratios are $m_e/m_p=0.08$ and $m_h/m_o=021$ [78].

The presence of recombination mechanisms, such as BI, BT, and BB, has been observed in different chalcogenide semiconductors, including p-type $CuGaSe_2$ and $CuIn_{1-x}Ga_xSe_2$. Although annealing techniques have been utilized to mitigate these mechanisms, they have not been entirely eliminated. The asymmetrical shape of the low-temperature wide PL bands is characterized by a peak position that experiences a rapid redshift with increasing temperature, reaching a minimum value at approximately 100–200 K. An observation was made in CZTSSe, revealed that the rate of the peak position redshift did not change as the laser power decreased [79]–[82].

Throughout investigations on ordered-disordered Kesterite by various methods such as the impact of Germanium incorporation on CZTSSe and the influence of Copper/Zinc content on CZTSe, similar recombination mechanisms are observed, and the PL bands are asymmetric Gaussian. PL band shows a steeper decline on the high-energy sides while demonstrating an exponential increase on the low-energy side. In contrast to ternary Chalcopyrite, the model of heavily doped semiconductor fit them and blueshift with an increase of excitation and redshift with an increase of temperature is common among them [78], [83]–[85].

An example of ordered-disordered phases coexistence in CZTS polycrystals is in [22] with two distinct PL bands detected at 1.27 eV and 1.35 eV at a temperature of T=10 K. Both PL bands exhibit similar characteristics regarding temperature and excitation power and are attributed to BI-recombination, and the peak at 1.35 eV arises from the Kesterite CZTS phase, while the PL band at 1.27 eV arises from the disordered Kesterite phase.

The presence of disordered Kesterite phase and compositional fluctuations lead to spatially varying bandgap energy and broadened PL bands due to the broadening of the density of states functions for electrons and holes. Local potential fluctuations induced by different surroundings of defect clusters can also contribute to this broadening by TI and TT recombination mechanisms. This behavior can be explained by the heavily doped semiconductor model [25]. It is well-established that in CZTSSe, the band gap energy can fluctuate by approximately 100-200 meV due to the varying Cu-Zn ordering ratio in the Kesterite lattice [6]. The primary loss mechanisms in Kesterite bulk are attributed to intrinsic properties such as the existence of defect clusters as recombination centers or the presence of band tails that restrict the effective energy of photogenerated carriers and their transport. Although it has been claimed that tail states only minimally decrease the V_{oc}, this is only

valid when radiative recombination is the main path, as tail states also contribute to non-radiative recombination, causing a further decrease in the room temperature V_{oc} [12].

This study will prioritize the investigation of the BI band, as it is the most frequently observed recombination pathway in Kesterite.

To proceed with additional measurements, the initial stage involves investigating the temperature dependence of the sample. This can be observed in Figure 3.6, which illustrates the variation in temperature ranging from 10 K to 200 K.
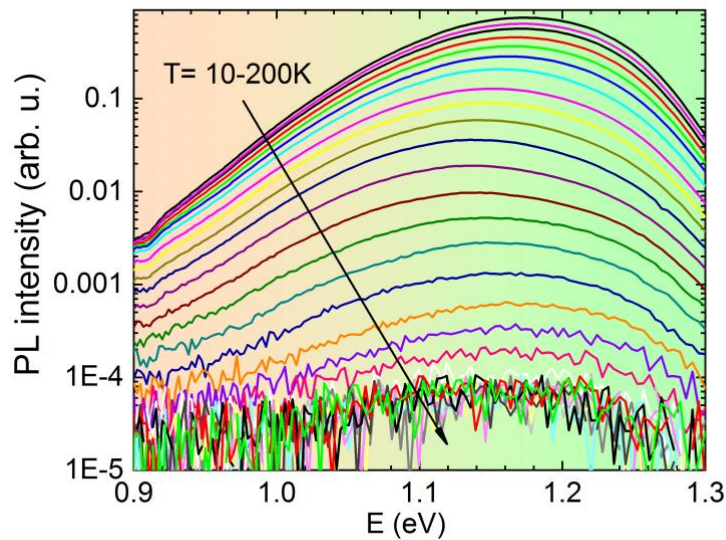
Figure 3.6: Temperature dependence of PL spectrum from CZTSSe microcrystal.

As the temperature increases, the low-energy (LE) side of the spectrum displays a broad PL band with a Gaussian shape containing a redshift in the peak positions. When the temperature is extremely low, optically produced electrons tend to get trapped near shallow energy wells in proximity to E_c. At this point, the quasi-Fermi level reaches its maximum position. As the temperature rises, the electrons present in these shallow states begin to migrate toward deeper potential wells. This migration process results in a redshift of the PL band peak position with increasing temperature [86]. Furthermore, as referred to in [86]–[88] the asymmetric PL band at low temperatures shows a sharper decay on the high-energy (HE) side.

As a general rule, the shape of the LE side of asymmetric PL bands at low temperatures is primarily determined by the density of states (DOS) function ρ(E), while the shape of the high-energy side of the PL band is largely influenced by temperature-dependent Fermi distribution function f(E). There are two proposed models regarding the treatment of tails caused by fluctuations. The first model considers the tails as defects (BI), which is only applicable for sufficiently deep fluctuations. In this case, the density of states is assumed to be Gaussian in shape. The second model treats the tails as Urbach tails (BT), which leads to a representation of the density of states as an exponential decay ([89]. Urbach tails appear in the optical absorption of various materials with different origins of disorder near the band edges. A possible explanation of these tails is presented, based on the

assumption that the absorption coefficient, $\alpha(E)$, is dependent on the photon energy, E. The energy dependence of $\alpha(E)$ is assumed to follow that of the density of electron states, $\rho(E)$, which has a tail reaching into the energy gap. When disorder has a correlation length approximately equal to the interatomic spacing and causes fluctuations in electron energies of the order of $\sim(eV)^2$, $\rho(E)$ has the Urbach exponential form in the energy range where Urbach tails are observed. Therefore, any material with these characteristics of disorder should exhibit Urbach tails [90].

The integral intensity Φ of the PL band exhibits a decrease with increasing temperature, and this decrease follows a straightforward exponential pattern according to the Arrhenius plot where the dependence of $\ln \Phi(T)$ versus 1000/T [91].

$$\Phi(T) = \frac{\Phi_0}{1 + \alpha_1 T^{3/2} + \alpha_2 T^{3/2} \exp\left(\frac{-E_A}{K_B T}\right)} \tag{3.2}$$

Where Φ is the integral intensity of the PL band, α_1, and α_2 are the process rate parameters, and E_A is the thermal activation energy. Activation energy is the energy required to overcome the potential energy barrier between the reactants and products and initiate the reaction. The activation energy can be provided in various forms, such as heat, light, or mechanical force. In thermal reactions, the activation energy is typically provided as heat, and the reaction rate increases with temperature due to more particles having the required energy to overcome the activation barrier [92]. The thermal activation energy of our sample is demonstrated in Figure 3.7 and E_A = 121 ± 8 meV suggesting that the PL emission is caused by acceptor defects that are relatively deep. Based on the provided table [17] and the S/Se ratio, it can be inferred that the Cu_{Zn} acceptor defect is the most likely defect involved, given the energy amount.
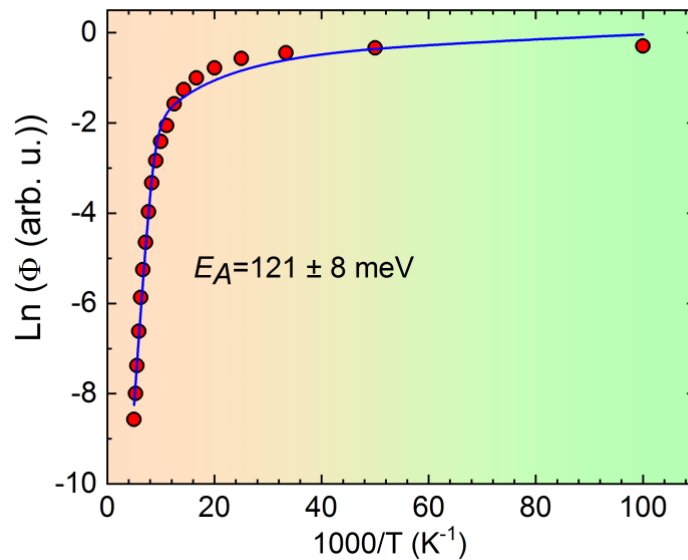
Figure 3.7: Equation (3.2) was used to fit the thermal quenching of integral intensity Φ.

The recombination mechanism expected in this context is the BI type, in which the occupation of acceptor levels is influenced by localized holes within potential wells created by bandgap and/or potential fluctuations, while electrons are considered free. It's worth noting that, at appropriate

temperatures and deeper bandgap fluctuations, electrons can also localize within potential wells created at the edge of the conduction band. The distribution of holes between potential wells with different depths is mainly influenced by the temperature. At very low temperatures, holes will mostly occupy shallow wells, giving rise to the HE part of the BI band. As the temperature increases, holes redistribute from shallow wells into deeper ones, causing the corresponding emission band to shift toward the LE. The presented Figure 3.8 illustrates a model of recombination for the BI band in CZTSSe microcrystals, where significant fluctuations in bandgap energy occur. It is important to note that the deeper potential wells for holes, as well as electrons, mainly impact the low-energy (LE) side of the PL band, whereas the shallow wells contribute more to the high-energy (HE) side. Redistribution of holes among different potential wells leads to a shift of the PL band towards the red and blue sides as temperature increases.
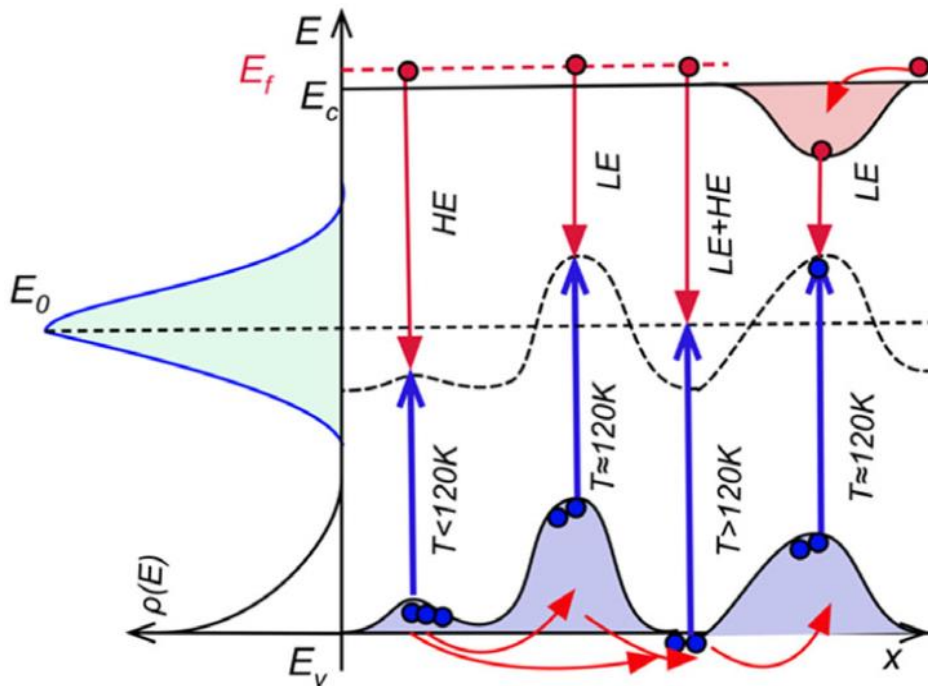
Figure 3.8: A schematic model to illustrate recombination models in CZTSSe with strong bandgap fluctuation.

As temperature increases, the PL band shifts towards the blue region as all the trapped holes become free and are captured by acceptor defects from the valence band. The distribution of these holes among various localized states impacts the shape and temperature dependence of the PL band, and comparable scenarios have been examined in other literature [93].

A distribution function for localized carriers is derived and a model for the luminescence of the localized-state ensemble (LSE) is developed in [94] for quantum dots with lattice temperature T. According to the model, the anomalies in the temperature dependence of the luminescence peak are caused by the thermal redistribution of localized carriers within the localized states.

$$I(E) \propto \rho(E).f(E) \tag{3.3}$$

while a distribution function can be considered

$$f(E,T) = \frac{1}{exp\left(\frac{E-E_a^*}{K_B T_e^*}\right) + \frac{\tau_{tr}}{\tau_r}}$$ (3.4)

For an LSE system with a Gaussian-type DOS, which may be caused by, e.g., fluctuations of alloy composition:

$$\rho(E) = \rho_0 \, exp\left[-\frac{(E-E_0)^2}{2\sigma^2}\right]$$ (3.5)

Where E_0 is a peak position and σ is the standard deviation of the distribution function of acceptor states, E_a^* represents a "marking" level, like a quasi-Fermi level, where all the localized states are filled with carriers, and T_e^* is an effective carrier temperature. In order to use the model for fitting the shape of the experimentally obtained PL band, it was necessary to apply the effective carrier temperature. While it is possible to extract a carrier temperature from the HE tail of the PL band in principle, the spectra can be broadened by phonon-related effects at higher lattice temperatures, hence the effective temperature is employed. As the depth of bandgap fluctuations increases, the significance of their role also increases. This implies that the carrier temperature obtained from PL spectra is typically higher than the actual carrier temperature. This difference is more prominent at higher temperatures. Hence, the term "effective carrier temperature" is utilized to account for this difference. The value of σ at T = 10 K is 79 meV, which can be considered as the average amplitude of fluctuations. In CZTSSe, the average depth of electrostatic potential fluctuations does not usually exceed 50 meV [65] indicating that bandgap fluctuations are likely the dominant factor in our sample. The reciprocal of τ_r represents the rate of radiative recombination, whereas the reciprocal of τ_{tr} denotes the rate at which localized carriers attempt to escape. According to Figure 3.9 the outline of the HE tail of the PL band is primarily influenced by T_e^*, while the width and extent of the distribution are affected by E_a^* and $\frac{\tau_{tr}}{\tau_r}$.
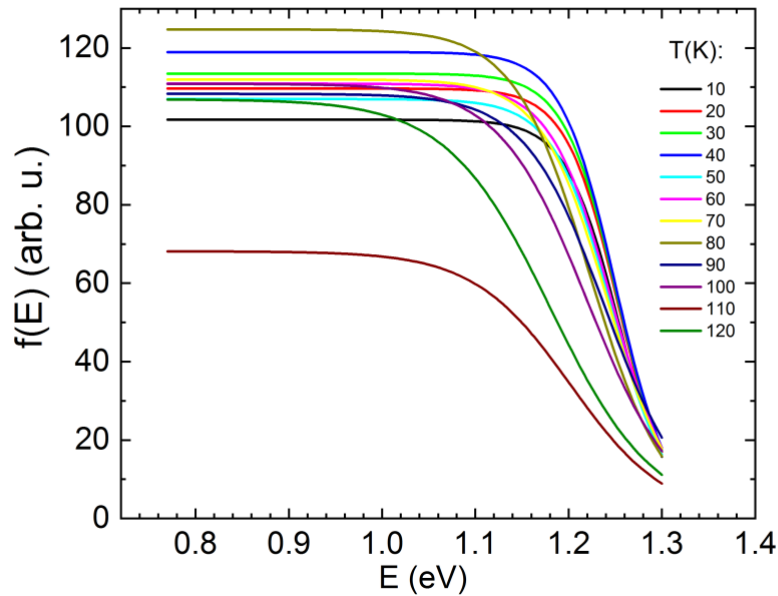
Figure 3.9: The temperature dependence of the shape of the f(E) function as determined by spectral fitting.

With the help of fitting with Equation (3.3) , the redshift of peak positions from 10 K to 120 K is depicted in Figure 3.10.
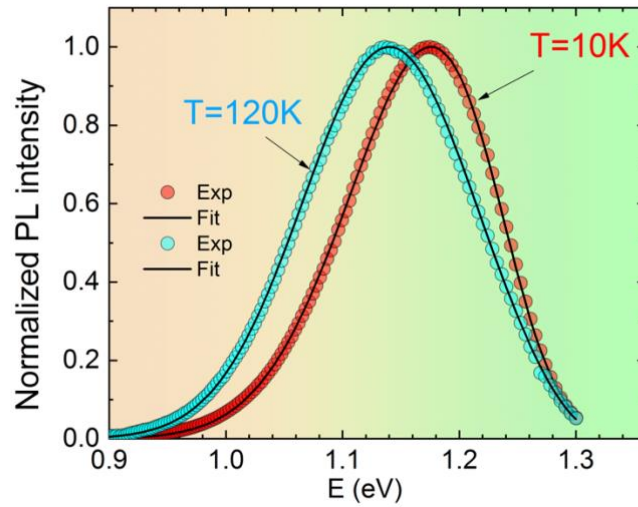
Figure 3.10: An illustration of fitting spectra using Equation (3.3) for two distinct temperatures

The position of the PL band peak, E_{max}, undergoes a significant redshift as the temperature increases, with the fastest redshift occurring at low temperatures, reaching a minimum value at T=130K, and then starting to increase again at T>130K.The rate of this redshift at low temperatures is greater than the rate of CZTS's bandgap energy E_g dependence shown in Figure 3.11.
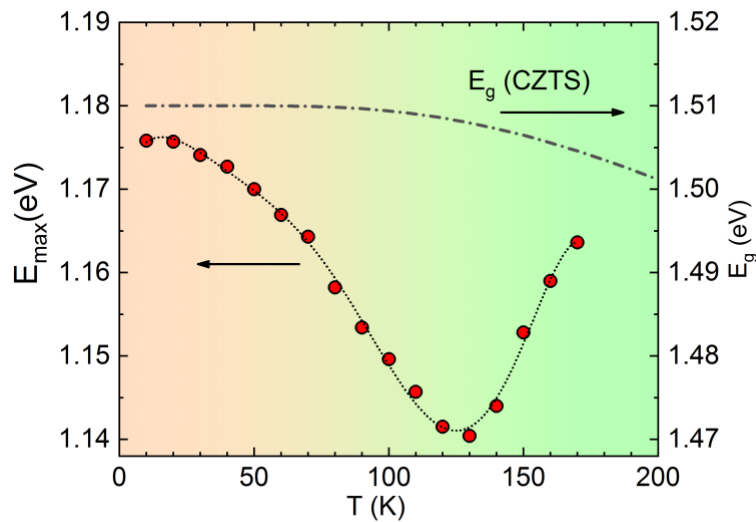
Figure 3.11: The variation of peak positions of PL emission, E_{max}, and the bandgap energy of CZTS [100] with temperature

It is assumed that the $E_g(T)$ dependence in the CZTSSe samples used has a similar rate.

Figure 3.12 shows the temperature dependence of the half width at half maximum for the HE and LE sides, represented as HWHM-H and HWHM-L, respectively.
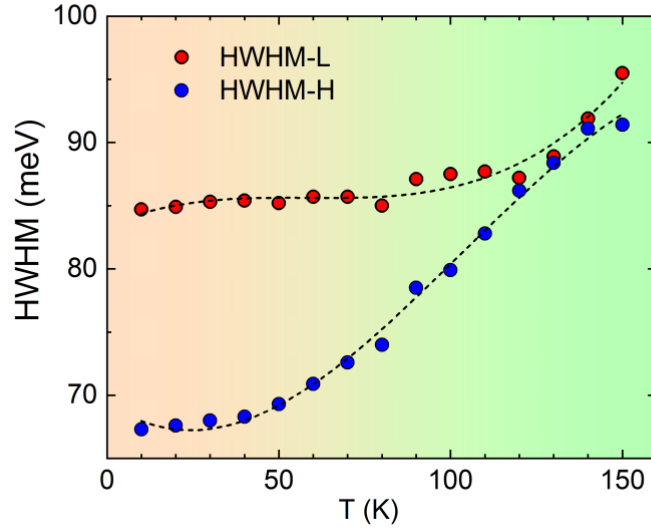
Figure 3.12: Temperature dependence of HWHM values for low- and high-energy sides of PL band

The increase in temperature causes rapid growth of HWHM-H due to electron-phonon interaction and the variation of T_e^*, value, while the HWHM-L shows only a slight increase due to the temperature-independent nature of the $\rho(E)$ function at low temperatures. As a result, the PL band becomes symmetrical and Gaussian in shape around T = 120 K, which is expected.

The next step is analyzing the full width at half maximum (FWHM) dependence on temperature. An unusually rapid increase in the FWHM value with temperature is observed, which cannot be explained solely by electron-phonon interaction. Therefore, we anticipate that bandgap fluctuations also play a role through the effective carrier temperature T_e^*. So, a model initially introduced by Lee et al.[95]can be used to identify the cause of the FWHM behavior with temperature in this case. Subsequently, the entire linewidth of the PL spectrum can be calculated using the formula:

$$FWHM(T) = W_0 + \frac{W_1}{[exp\left(\frac{\hbar w_{LO}}{K_B T}\right)-1]} + W_2 exp\left(-\frac{E_{fl}}{K_B T}\right) \qquad (3.6)$$

Equation 3.6 consists of three terms. The first term represents inhomogeneous broadening, the second term represents the interaction between carriers and optical phonons $\hbar w_{LO}$ is LO-phonon energy and is 41 meV for CZTS [73], then the third term represents the contribution of bandgap fluctuations to the broadening of the PL spectra. The parameter E_{fl} represents the average depth of the potential wells, which can be thought of as the strength of the fluctuations in the system. As the temperature increases, shallower wells will be emptied, and deeper wells will become more significant, resulting in a wider energy distribution of potential wells and an increase in the linewidth of the PL band. Since the interaction with acoustic phonons is typically insignificant, it wasn't included. Atoms vibrate around their equilibrium positions in solid materials, and these vibrations result in phonons. Lattice vibrations that can convey energy and momentum are known

as phonons. Solids include two different kinds of phonons: The atoms in the lattice move out of phase, with one moving to the left and its neighbor to the right, forming optical phonons. This happens if there are two or more atoms in the lattice basis. Because ionic crystal displacement fluctuations produce an electrical polarization that relates to the electromagnetic field, they are known as optical crystals. Since they are susceptible to being activated by the electric field of the light, the crystal will vibrate as every positive ion moves in the direction of the field and every negative ion moves in the opposite way. The energies of optical phonons match those of the photons that are absorbed or released during contact. A change in the longitudinal polarization of the lattice along the direction of wave propagation is what longitudinal optical phonons (LO phonons) do. On the other hand, acoustic phonons are the coherent motions of lattice atoms away from their equilibrium positions. Atoms will be closer in some places and farther apart in others if the displacement is in the direction of propagation. Similar to waves on a string, displacement is perpendicular to the propagation direction. With longer wavelengths, acoustic phonon frequencies tend to zero off. Acoustic phonons often have substantially lower energies than optical phonons [92], [96] .
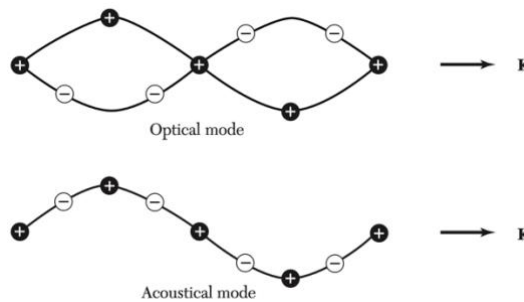
Figure 3.13: *A schematic illustration of Optical and Acoustic modes inside microcrystals* [92]

The parameters were used for fitting and the outcome is depicted in Figure 3.14. The E_{fl} = 14.8 meV is aligning with previous studies [97], which reported a similar energy range of 10 to 16 meV.
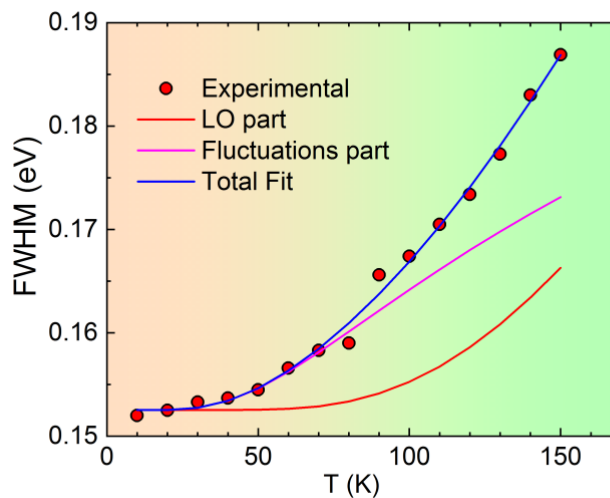
Figure 3.14: *Temperature dependence of FWHM and the result of fitting using Equation (3.6).*

The notion behind effective carrier temperature implies that the energy distribution of charge carriers can be described by the Fermi-Dirac distribution, but the effective carrier temperature T_e^* is higher than the lattice temperature T, due to the relatively short minority photocarrier lifetime τ, i.e., $T_e^* \sim \tau^{-1}$, a measure of recombination losses. The absorber of a hot carrier cell consists of a semiconductor with a narrow electronic band gap, allowing it to absorb a wide range of photon energies and give a high current. The majority of semiconductor materials have a hot carrier population of photogenerated electron-hole pairs, with most of the energy of the absorbed photons in the hot electrons, because of the small effective mass of electrons compared to holes. Hole dynamics are qualitatively similar but less important for energy extraction. However, in some compounds with a large difference in constituent element mass, there exists a large gap in the phonon dispersion between acoustic and optical phonon energies. An ideal hot carrier cell absorbs a wide range of photon energies and extracts a large fraction of the energy, resulting in high efficiencies close to the maximum thermodynamic limit, up to 65% at 1sun (85% at max concentration), by extracting 'hot' carriers before they thermalize to the band edges [98], [99]. The minority carrier lifetime (τ) is a critical parameter that determines the absorber quality of semiconductors. It measures the net recombination rate of minority carriers in a material, which can vary widely depending on the origin of limiting recombination. Therefore, it is important to identify and eliminate various loss mechanisms that hinder the improvement of τ. The carrier transport properties, including carrier type, density, and mobility, are fundamental to all optoelectronic devices. For CZTSSe, a range of carrier properties have been reported, reflecting changes in stoichiometry, doping, fabrication method, and sample quality, as well as the choice of characterization method. If the minority carrier lifetime is very short, excited carriers with high temperatures will recombine before they can "cool down" to the lattice temperature T due to carrier-phonon interaction and carrier-carrier scattering. Kesterite compounds exhibit an extremely small actual lifetime of photoexcited carriers, not exceeding values of hundreds of picoseconds. Accurate determination of τ is quite challenging for highly defective materials like Kesterites, owing to their complex carrier transport and dynamics, as well as high recombination rates. For this reason, we anticipate high values of T_e^* [17], [100].

Equation (3.7) shows that the effective carrier temperature increases at low temperatures [86] :

$$T_e^*(T) = T_0^* + \frac{a_1}{[exp\left(\frac{a_2}{K_B T}\right)-1]} \tag{3.7}$$

Where T_0^*, a_1, and a_2 are fitting parameters and Figure 3.15 is depicted based on them. As the temperature decreases, T_e^* increases while τ decreases, which is a common trend for various types of recombinations. At T = 110 K, T_e^* experiences a sudden decrease, indicating a shift in the recombination process. This is because all localized holes become unbound in this temperature range, leading to a change in the way holes are captured by acceptor levels.
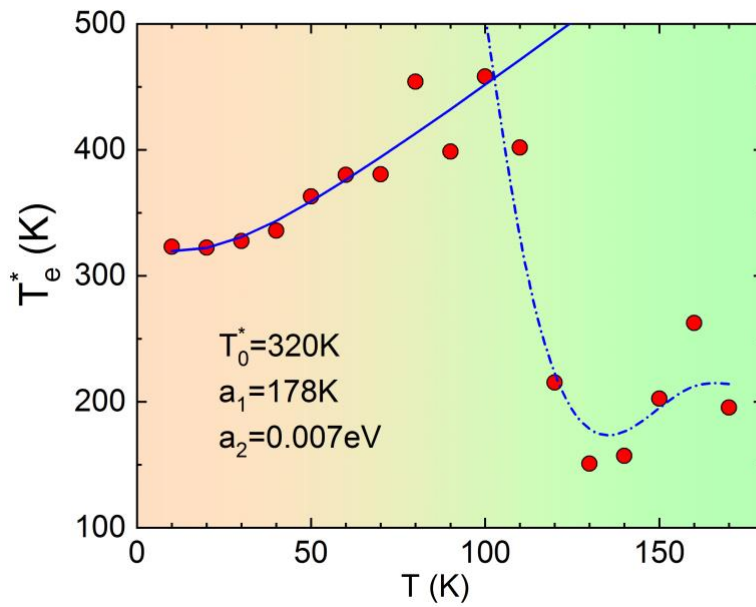
Figure 3.15: *The temperature dependence of an effective carrier temperature and fitting result with Equation (3.7).*

The laser power dependency measurements at T=10 K was done on our sample and its PL spectrum is demonstrated in Figure 3.16 containing excitation change from 0.26 mW to 37.1 mW.
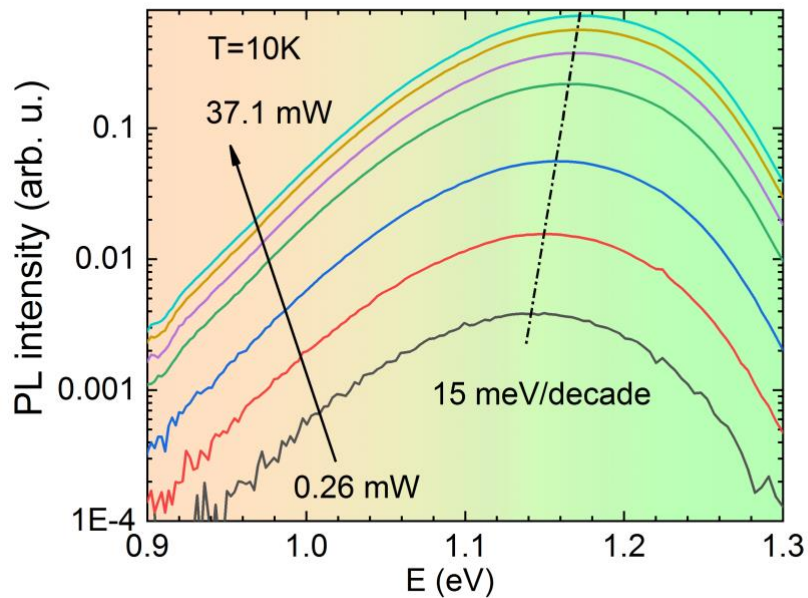
Figure 3.16: *The laser dependence of CZTSSe spectra at T =10 K demonstrates a blueshift of peak positions*

The PL band peak position exhibits a blueshift of 15 meV per decade of laser power, which is a characteristic feature of semiconductor materials with potential and/or bandgap fluctuations. The observed blueshift can be attributed to the band-filling effect and/or the decrease in the effective carrier temperature with laser power.

The behavior of T_e^* at 10 K under various laser power is shown in Figure 3.17.
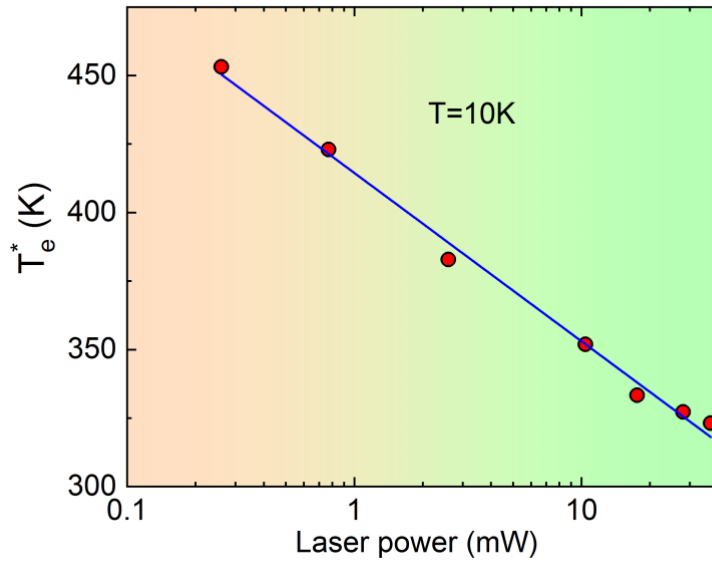
Figure 3.17: *The laser dependency of the effective carrier temperature.*

It has been perceived that the effective carrier temperature T_e^* decreases linearly with increasing laser power. This trend indicates a longer carrier lifetime through the constant increase of laser power.

The recombination rate, which is a function of excess carrier density, can be determined by summing the radiative, SRH, and Auger recombination rates. Subsequently, the minority carrier lifetime can be determined [101].

$$\frac{1}{\tau} = \frac{1}{\tau_{rad}} + \frac{1}{\tau_{Aug}} + \frac{1}{\tau_{SRH}}$$

(3.8)

Where τ_{rad} is radiative recombination lifetime, τ_{Aug} is a lifetime related to Auger recombination, and τ_{SRH} is a defect-related Shokley-Read-Hall (SRH) recombination lifetime.

Radiative recombination is the dominant mechanism for recombination in direct bandgap semiconductors. It involves the direct combination of an electron from the conduction band with a hole in the valence band, which emits a photon. The emitted photon has a similar energy to the band gap, making it weakly absorbed and capable of exiting the semiconductor. Moreover, recombination through defects, or SRH, involves a trap level or a defect energy level within the band gap. This two-step process begins with an electron (or hole) being trapped by an energy state in the forbidden region, which is introduced through defects in the crystal lattice. If a hole (or an electron) moves up to the same energy state before the electron is thermally re-emitted into the conduction band, then it recombines. The carrier's rate of movement into the energy level in the forbidden gap is determined by the distance of the introduced energy level from either of the band edges. For this reason, energy levels close to either band edge reduce recombination since the electron is more likely to be re-emitted to the conduction band edge than recombine with a hole

moving into the same energy state from the valence band. Mid-gap energy levels are very efficient for recombination. Finally, the process of Auger Recombination involves the participation of three carriers, wherein an electron and a hole recombine, but instead of releasing energy as heat or photon, a third carrier, an electron in the conduction band receives the energy, and then returns to the conduction band edge through thermalization. The lifetime of Auger recombination decreases as the material becomes more heavily doped [102]–[104].

In a classical study of SRH recombination [103], it was found that the lifetime of minority carriers caused by SRH recombination can increase under certain conditions, specifically with excess carrier concentration or increasing laser power. This contrasts with other types of recombination where the lifetime typically decreases with increasing laser power [101]. Therefore, the decrease of T_e^* with laser power is attributed to the dominance of nonradiative SRH recombination at low temperatures.

4. CONCLUSION

The aim of this study was to investigate the recombination mechanisms related to intrinsic defects of disordered CZTSSe microcrystals with the help of PL measurements. The spectrum we obtained is consistent with similar spectra found in the literature investigating order-disorder Kesterite. An asymmetric Gaussian spectrum exhibits a blueshift of peak positions as excitation increases and a redshift as temperature grows. The behavior of heavily doped semiconductors is significantly affected by the masses of electrons and holes due to the overlapping wave functions of these defects, resulting in a high doping concentration. The luminescence of these materials is governed not only by BB, BT, and BI transitions but also by TI and TT transitions. The high-energy side of the Kesterite PL band exhibits a sharp drop, whereas the low-energy side demonstrates an exponential rise. The presence of the disordered Kesterite phase and compositional fluctuations results in spatially varying bandgap energy by approximately 100-200 meV and broadened PL bands. This is due to the broadening of the density of state functions for electrons and holes, as well as local potential fluctuations induced by different defect cluster surroundings. CZTSSe is subject to band gap energy fluctuations due to the varying Cu-Zn ordering ratio. The primary loss mechanisms in Kesterite bulk are attributed to intrinsic properties such as the existence of defect clusters as recombination centers or the presence of band tails that restrict the effective energy of photogenerated carriers and their transport. The primary focus of this study was to examine the BI band, which is the most observed recombination pathway in Kesterite. To further investigate, the first step was to analyze the temperature dependence of the sample ranging from 10 K to 200 K. At extremely low temperatures, optically produced electrons are trapped near shallow energy wells and the quasi-Fermi level reaches its maximum position. As the temperature increases, the electrons start to move towards deeper potential wells, leading to a redshift in the peak position of the LE of the spectrum. As per previous studies, the asymmetric PL band displays a sharper decay on the HE at low temperatures. The most likely acceptor defect in our sample is Cu_{Zn}, based on the thermal activation energy of $E_A = 121 \pm 8$ meV, which suggests the presence of relatively deep acceptor defects. The researchers derived a distribution function for localized carriers and proposed a model for luminescence of the localized-state ensemble in quantum dots, with a lattice temperature of T. The model assumes that all localized states are filled with carriers, and introduces an effective carrier temperature, T_e^*. To fit the experimentally obtained PL band, the effective carrier temperature needed to be applied. The dominant factor is likely the bandgap fluctuations, as indicated by the average amplitude of fluctuations in our sample at 10 K, which was measured to be 79 meV. The E_{max} in CZTSSe undergoes a substantial redshift as the temperature rises, with the most rapid shift occurring at low temperatures, reaching a minimum value at T=130K, and then beginning to increase again at T>130K. It was assumed that the $E_g(T)$ of CZTSSe samples used have a similar rate to CZTS one. The effective carrier temperature is higher than the lattice temperature due to the short photocarrier lifetime, which results in recombination losses. The Kesterite compounds have a short lifetime of photoexcited carriers which is difficult to determine due to complex transport and dynamics, leading to high recombination rates. This indicates high values of T_e^*. At a temperature of 110 K, T_e^* experiences a sudden decrease, indicating a shift in the recombination process.

The position of the PL band peak undergoes a blueshift of 15 meV per decade of laser power, which is a characteristic of semiconductors with potential and/or bandgap fluctuations. This blueshift can be caused by the band-filling effect and/or the decrease in T_e^* with laser power. The lifetime of minority carriers caused by SRH recombination can increase under certain conditions, such as excess carrier concentration or increasing laser power, according to a classical study of SRH recombination. This contrasts with other types of recombination where the lifetime usually decreases with increasing laser power. As a result, the decrease of the effective carrier temperature with laser power is attributed to the prevalence of nonradiative SRH recombination at low temperatures.

In summary, the photoluminescence band of highly doped CZTSSe synthesized under Cu-poor Zn-rich condition suggests that the presence of both disordered and ordered phases in these microcrystals results in significant bandgap fluctuations and recombination mechanisms' rate. As a result, there is a short lifetime of photoexcited carriers and high effective temperature of them, which ultimately leads to relatively low V_{oc} and efficiency.

The findings of this study on the photoluminescence of CZTSSe, have been published in a paper titled 'Bandgap Fluctuations, Hot Carriers, and Band-to-Acceptor Recombination in $Cu_2ZnSn(S,Se)_4$ Microcrystals' by Professor Jüri Krustok, Reelika Kaupmees, Nafiseh Abbasi, Katri Muska, Idil Mengü, and Kristi Timmo in Physica Status Solidi-Rapid Research Letters journal, doi: 10.1002/pssr.202300077, 2023. The full citation of this paper is included in the reference section of this thesis [105]. A copy of the published paper can also be found in the appendix.

SUMMARY

The aim of this master's thesis is to investigate the defect structure and related recombination mechanisms in disordered CZTSSe monograin powders by utilizing Raman and photoluminescence spectroscopy. According to synthesizing steps, three samples named as-grown, etched, and annealed were analyzed.

EDX analysis showed that the crystals had a Cu-poor Zn-rich elemental composition, and the distribution of elements was homogeneous across all crystals with no significant fluctuations observed. The room-temperature Raman spectroscopy was utilized to study the phase composition and structural quality of the monograins. Each sample spectrum contained 11 individual peaks. The ZnSe secondary phase was identified the was confirmed by EDX analysis too.

Photoluminescence measurements were conducted at room temperature and 8 K for all three samples. The annealed sample showed significantly larger peak intensities, particularly on the higher energy side, which suggests its potential as the most interesting sample to delve deeper into.

Further investigation into the recombination mechanisms of the disordered annealed sample was conducted by performing temperature-dependent photoluminescence measurements from 10 K to 200 K. By utilizing a modified localized-state ensemble model, the resulting spectra displayed the typical asymmetric Gaussian shape for Kesterite and revealed a redshift with increasing temperature. This PL band's temperature dependence is shown to be affected by the transfer of holes between valence band potential wells of different depths.The main recombination mechanism was found to be BI, with an average fluctuation amplitude of σ= 79 meV, highlighting the significant band fluc'uations present in our sample. The CZTSSe microcrystals exhibited a thermal activation energy of E_A = 121 ± 8 meV, indicating that the PL emission is likely caused by relatively deep acceptor defects. Based on the activation energy range, it is likely that the Cu_{Zn} acceptor defect is the most plausible candidate for the observed defect. The introduction of an effective carrier temperature (T_e^*) allows for a good fit of the band shape at different temperatures. The temperature was found to be about 300 K higher than the lattice temperature in the samples, primarily due to the extremely short minority carrier lifetime. A trend was observed in its behavior, indicating that its value increases with decreasing temperature. However, a sudden decline in the effective temperature after T = 110 K suggests a shift in the recombination process. Upon varying the laser power from 0.26 to 37.1 mW, a characteristic blueshift of peak position by 15 meV per decade was observed, which is indicative of potential and/or bandgap fluctuations in the semiconductor material. The observed blueshift may be attributed to either the band-filling effect or the decrease in effective carrier temperature with laser power. At the end of the analysis, the minority carrier lifetime was determined, revealing that the decrease in T_e^* with laser power can be attributed to the prevalence of nonradiative SRH recombination at low temperatures.

REFERENCES

[1]   BDO Global, 'The near future of renewables', 2023. https://www.bdo.global/en-gb/industries-en/natural-resources-energy/the-near-future-of/2023-the-near-future-of-renewables (accessed May 05, 2023).

[2]   M. de, 'Snapshot of Global PV Markets 2023 Task 1 Strategic PV Analysis and Outreach PVPS', 2023. [Online]. Available: www.iea-pvps.org

[3]   C. Candelise, J. F. Spiers, and R. J. K. Gross, 'Materials availability for thin film (TF) PV technologies development: A real concern?', *Renewable and Sustainable Energy Reviews*, vol. 15, no. 9. pp. 4972–4981, Dec. 2011. doi: 10.1016/j.rser.2011.06.0127.

[4]   W. Wang *et al.*, 'Device characteristics of CZTSSe thin-film solar cells with 12.6% efficiency', *Adv Energy Mater*, vol. 4, no. 7, May 2014, doi: 10.1002/aenm.201301465.

[5]   T. Ratz *et al.*, 'Physical routes for the synthesis of kesterite', *JPhys Energy*, vol. 1, no. 4. IOP Publishing Ltd, Oct. 01, 2019. doi: 10.1088/2515-7655/ab281c.

[6]   G. Rey *et al.*, 'The band gap of $Cu_2ZnSnSe_4$: Effect of order-disorder', *Appl Phys Lett*, vol. 105, no. 11, Sep. 2014, doi: 10.1063/1.4896315.

[7]   J. Krustok *et al.*, 'Study of point defects in wide-bandgap Cu_2CdGeS_4 microcrystals by temperature and laser power dependent photoluminescence spectroscopy', *J Phys D Appl Phys*, vol. 53, no. 27, Jul. 2020, doi: 10.1088/1361-6463/ab83c1.

[8]   V. Fthenakis, 'Sustainability of photovoltaics: The case for thin-film solar cells', *Renewable and Sustainable Energy Reviews*, vol. 13, no. 9. pp. 2746–2750, Dec. 2009. doi: 10.1016/j.rser.2009.05.001.

[9]   United Nations Environment Programme, *Green energy choices : the benefits, risks and trade-offs of low-carbon technologies for electricity production.*

[10]   Hannah Ritchie and Max Roser and Pablo Rosado, 'Energy', *Our World in Data*, 2022. https://ourworldindata.org/energy-mix#:~:text=As%20we%20look%20at%20in,than%2080%25%20of%20energy%20consumption.

[11]   J. Li, D. Wang, X. Li, Y. Zeng, and Y. Zhang, 'Cation Substitution in Earth-Abundant Kesterite Photovoltaic Materials', *Advanced Science*, vol. 5, no. 4. Wiley-VCH Verlag, Apr. 01, 2018. doi: 10.1002/advs.201700744.

[12]   G. Rey *et al.*, 'On the origin of band-tails in kesterite', *Solar Energy Materials and Solar Cells*, vol. 179, pp. 142–151, Jun. 2018, doi: 10.1016/j.solmat.2017.11.005.

[13]   S. Siebentritt and T. P. Weiss, 'Chalcopyrite solar cells —state-of-the-art and options for improvement', *Science China: Physics, Mechanics and Astronomy*, vol. 66, no. 1. Science Press (China), Jan. 01, 2023. doi: 10.1007/s11433-022-2001-4.

[14]   S. Siebentritt, A. Lomuscio, D. Adeleye, M. Sood, and A. Dwivedi, 'Sulfide Chalcopyrite Solar Cells—Are They the Same as Selenides with a Wider Bandgap?', *Physica Status Solidi - Rapid Research Letters*, vol. 16, no. 8. John Wiley and Sons Inc, Aug. 01, 2022. doi: 10.1002/pssr.202200126.

[15]   S. Saha, 'A Status Review on $Cu_2ZnSn(S, Se)_4$-Based Thin-Film Solar Cells', *International Journal of Photoenergy*, vol. 2020. Hindawi Limited, 2020. doi: 10.1155/2020/3036413.

[16]   S. Giraldo, Z. Jehl, M. Placidi, V. Izquierdo-Roca, A. Pérez-Rodríguez, and E. Saucedo, 'Progress and Perspectives of Thin Film Kesterite Photovoltaic Technology: A Critical Review', *Advanced Materials*, vol. 31, no. 16. Wiley-VCH Verlag, Apr. 19, 2019. doi: 10.1002/adma.201806692.

[17]   M. Grossberg *et al.*, 'The electrical and optical properties of kesterites', *JPhys Energy*, vol. 1, no. 4, Oct. 2019, doi: 10.1088/2515-7655/ab29a0.

[18]   T. Schwarz *et al.*, 'Atom probe study of Cu2ZnSnSe4 thin-films prepared by co-evaporation and post-deposition annealing', *Appl Phys Lett*, vol. 102, no. 4, Jan. 2013, doi: 10.1063/1.4788815.

[19]   M. Pilvet, 'Study of Cu 2 (Zn,Cd)SnS 4 Absorber Materials for Monograin Layer Solar Cells', 2017.

[20]   D. Meissner *et al.*, 'Kesterite based monograin photovoltaics: The ideal solution for sustainable power supply', *Solar Energy Materials and Solar Cells*, vol. 252, Apr. 2023, doi: 10.1016/j.solmat.2022.112160.

[21]   M. Altosaar *et al.*, 'Monograin layer solar cells', in *Thin Solid Films*, May 2003, pp. 466–469. doi: 10.1016/S0040-6090(03)00167-6.

[22]   M. Grossberg, J. Krustok, J. Raudoja, and T. Raadik, 'The role of structural properties on deep defect states in Cu 2ZnSnS 4 studied by photoluminescence spectroscopy', *Appl Phys Lett*, vol. 101, no. 10, Sep. 2012, doi: 10.1063/1.4750249.

[23]   J. Krustok, T. Raadik, M. Grossberg, M. Kauk-Kuusik, V. Trifiletti, and S. Binetti, 'Photoluminescence study of deep donor- deep acceptor pairs in Cu2ZnSnS4', *Mater Sci Semicond Process*, vol. 80, pp. 52–55, Jun. 2018, doi: 10.1016/j.mssp.2018.02.025.

[24]   X. Zhang, E. Fu, Y. Wang, and C. Zhang, 'Fabrication of Cu 2 ZnSnS 4 (CZTS) nanoparticle inks for growth of CZTS films for solar cells', *Nanomaterials*, vol. 9, no. 3, Mar. 2019, doi: 10.3390/nano9030336.

[25]   M. Grossberg, T. Raadik, J. Raudoja, and J. Krustok, 'Photoluminescence study of defect clusters in Cu2ZnSnS 4 polycrystals', *Current Applied Physics*, vol. 14, no. 3, pp. 447–450, Mar. 2014, doi: 10.1016/j.cap.2013.12.029.

[26]   E. Kask, T. Raadik, M. Grossberg, R. Josepson, and J. Krustok, 'Deep defects in Cu 2ZnSnS 4 monograin solar cells', in *Energy Procedia*, 2011, pp. 261–265. doi: 10.1016/j.egypro.2011.10.188.

[27]   M. Danilson *et al.*, 'Temperature dependent current transport properties in Cu2ZnSnS4solar cells', *Thin Solid Films*, vol. 582, pp. 162–165, May 2015, doi: 10.1016/j.tsf.2014.10.069.

[28]   R. B. Wexler, G. S. Gautam, and E. A. Carter, 'Optimizing kesterite solar cells from Cu2ZnSnS4to Cu2CdGe(S,Se)4', *J Mater Chem A Mater*, vol. 9, no. 15, pp. 9882–9897, Apr. 2021, doi: 10.1039/d0ta11603c.

[29]   K. Hönes, E. Zscherpel, J. Scragg, and S. Siebentritt, 'Shallow defects in Cu2ZnSnS4', *Physica B Condens Matter*, vol. 404, no. 23–24, pp. 4949–4952, Dec. 2009, doi: 10.1016/j.physb.2009.08.206.

[30]   M. Dimitrievska *et al.*, 'Multiwavelength excitation Raman scattering study of polycrystalline kesterite Cu2ZnSnS4 thin films', *Appl Phys Lett*, vol. 104, no. 2, Jan. 2014, doi: 10.1063/1.4861593.

[31]   S. T. Yussuf, K. C. Nwambaekwe, M. E. Ramoroka, and E. I. Iwuoha, 'Photovoltaic efficiencies of microwave and Cu2ZnSnS4 (CZTS) superstrate solar cells', *Materials Today Sustainability*, vol. 21. Elsevier Ltd, Mar. 01, 2023. doi: 10.1016/j.mtsust.2022.100287.

[32]   H. Katagiri *et al.*, 'Development of CZTS-based thin film solar cells', *Thin Solid Films*, vol. 517, no. 7, pp. 2455–2460, Feb. 2009, doi: 10.1016/j.tsf.2008.11.002.

[33]   L. S. Khanzada, M. A. Makhdoom, X. Lin, H. Azimi, and C. J. Brabec, 'Photocurrent generation and charge transport mechanism study in solution-processed CZTS thin films', *Optik (Stuttg)*, vol. 272, Feb. 2023, doi: 10.1016/j.ijleo.2022.170381.

[34]   S. Padhy, R. Mannu, and U. P. Singh, 'Graded band gap structure of kesterite material using bilayer of CZTS and CZTSe for enhanced performance: A numerical approach', *Solar Energy*, vol. 216, pp. 601–609, Mar. 2021, doi: 10.1016/j.solener.2021.01.057.

[35]   M. V. Yakushev *et al.*, 'Optical spectroscopy studies of Cu2ZnSnSe4thin films', in *Thin Solid Films*, Elsevier B.V., May 2015, pp. 154–157. doi: 10.1016/j.tsf.2014.09.010.

[36]   M. A. Sulimov *et al.*, 'A PL and PLE Study of High Cu Content Cu2ZnSnSe4 Films on Mo/Glass and Solar Cells', *Physics of the Solid State*, vol. 61, no. 5, pp. 908–917, May 2019, doi: 10.1134/S1063783419050214.

[37]   F. Luckert *et al.*, 'Optical properties of high quality Cu 2ZnSnSe 4 thin films', *Appl Phys Lett*, vol. 99, no. 6, Aug. 2011, doi: 10.1063/1.3624827.

[38]   J. Krustok *et al.*, 'Temperature dependent electroreflectance study of Cu2ZnSnSe4 solar cells', *Mater Sci Semicond Process*, vol. 39, pp. 251–254, Jun. 2015, doi: 10.1016/j.mssp.2015.04.055.

[39]   E. Kask, J. Krustok, S. Giraldo, M. Neuschitzer, S. López-Marino, and E. Saucedo, 'Temperature dependent electrical characterization of thin film Cu2ZnSnSe4 solar cells', *J Phys D Appl Phys*, vol. 49, no. 8, Jan. 2016, doi: 10.1088/0022-3727/49/8/085101.

[40]   M. Grossberg, J. Krustok, K. Timmo, and M. Altosaar, 'Radiative recombination in Cu2ZnSnSe4 monograins studied by photoluminescence spectroscopy', *Thin Solid Films*, vol. 517, no. 7, pp. 2489–2492, Feb. 2009, doi: 10.1016/j.tsf.2008.11.024.

[41]   M. A. Sulimov *et al.*, 'Effects of irradiation of ZnO/CdS/Cu2ZnSnSe4/Mo/glass solar cells by 10 MeV electrons on photoluminescence spectra', *Mater Sci Semicond Process*, vol. 121, Jan. 2021, doi: 10.1016/j.mssp.2020.105301.

[42]   Tetiana Olar, 'Assessment of kesterite electronic and chemical surface properties', 2017.

[43]   A. Wang, M. He, M. A. Green, K. Sun, and X. Hao, 'A Critical Review on the Progress of Kesterite Solar Cells: Current Strategies and Insights', *Advanced Energy Materials*, vol. 13, no. 2. John Wiley and Sons Inc, Jan. 13, 2023. doi: 10.1002/aenm.202203046.

[44]   S. Siebentritt and S. Schorr, 'Kesterites-a challenging material for solar cells', *Progress in Photovoltaics: Research and Applications*, vol. 20, no. 5, pp. 512–519, Aug. 2012, doi: 10.1002/pip.2156.

[45]   T. Schwarz *et al.*, 'Variable chemical decoration of extended defects in Cu-poor C u2ZnSnS e4 thin films', *Phys Rev Mater*, vol. 3, no. 3, Mar. 2019, doi: 10.1103/PhysRevMaterials.3.035402.

[46]   G. Altamura, 'Development of CZTSSe thin films based solar cells"', 2014. [Online]. Available: https://theses.hal.science/tel-01060095

[47]   A. Crossay, 'EN CHIMIE ELECTRODEPOSITION AND SELENIZATION OF METALLIC THIN FILMS FOR KESTERITE SOLAR CELLS APPLICATION', 2016.

[48]   D. P. Zarceño, 'Improving kesterite for its use in low-cost superstrate solar cells', 2022.

[49]   M. M. A. Abusnina, 'Synthesis and Characterization of Kesterite Cu2ZnSnS4 (CZTS) Thin Films for Solar Cell Application Thin Films for Solar Cell Application', 2016. [Online]. Available: https://digitalcommons.du.edu/etd

[50]   J. T. Gibbon, 'Band Alignments and Interfaces in Kesterite Photovoltaics', 2018.

[51] J. J. S. Scragg *et al.*, 'Cu-Zn disorder and band gap fluctuations in Cu2ZnSn(S,Se)4: Theoretical and experimental investigations', *Phys Status Solidi B Basic Res*, vol. 253, no. 2, pp. 247–254, Feb. 2016, doi: 10.1002/pssb.201552530.

[52] von Dipl-Phys Christoph Daniel Krämmer aus Karlsruhe, H. M. Kalt Priv-Doz Hetterich A Shnirman Priv-Doz S Gieseke T Müller, and C. Daniel Krämmer, 'Optoelectronic Characterization of Thin-Film Solar Cells by Electroreflectance and Luminescence Spectroscopy', 2015.

[53] Mengü, J. Krustok, R. Kaupmees, V. Mikli, M. Kauk-Kuusik, and M. Grossberg-Kuusk, 'Radiative recombination pathways in ordered and disordered CZTSe microcrystals', *Mater Chem Phys*, vol. 301, Jun. 2023, doi: 10.1016/j.matchemphys.2023.127685.

[54] Y. Gong *et al.*, 'Ag Incorporation with Controlled Grain Growth Enables 12.5% Efficient Kesterite Solar Cell with Open Circuit Voltage Reached 64.2% Shockley–Queisser Limit', *Adv Funct Mater*, vol. 31, no. 24, Jun. 2021, doi: 10.1002/adfm.202101927.

[55] S. Siebentritt *et al.*, 'Photoluminescence assessment of materials for solar cell absorbers', *Faraday Discuss*, vol. 239, pp. 112–129, Jun. 2022, doi: 10.1039/d2fd00057a.

[56] Seyyedmahan Khatami, 'STUDY OF OPTOELECTRONIC PROPERTIES OF Cu 2 Zn(Sn,Sb)S 4 MONOGRAIN POWDERS AND CORRESPONDING SOLAR CELLS', 2021.

[57] Katja M. HÖNES, 'PHOTOLUMINESCENCEMEASUREMENTSONSOLARCELLMATERIALS: CHALCOPYRITESANDKESTERITES', 2011.

[58] Y. ALTOWAIRQI, 'Copper Zinc Tin Sulphide (Cu2ZnSnS4) Nanoparticle Ink Solar Cells', 2019. [Online]. Available: http://etheses.dur.ac.uk/13162/

[59] Mowafak Al-Jassim and Nancy Haege, *Advanced characterization of thin film solar cells*. 2020.

[60] K. Timmo *et al.*, 'The effect of Ag alloying of Cu2(Zn,Cd)SnS4 on the monograin powder properties and solar cell performance', *J Mater Chem A Mater*, vol. 7, no. 42, pp. 24281–24291, 2019, doi: 10.1039/c9ta07768e.

[61] J. He, L. Sun, S. Chen, Y. Chen, P. Yang, and J. Chu, 'Composition dependence of structure and optical properties of Cu 2ZnSn(S,Se)4 solid solutions: An experimental study', *J Alloys Compd*, vol. 511, no. 1, pp. 129–132, Jan. 2012, doi: 10.1016/j.jallcom.2011.08.099.

[62] A. Fairbrother, 'Development of Cu 2 ZnSn(S,Se) 4 based solar cells', 2014. [Online]. Available: www.tdx.cat

[63] J. Kim *et al.*, 'Photo-excited carrier transport and secondary phases of Na-engineered kesterite flexible thin films', *Solar Energy Materials and Solar Cells*, vol. 250, Jan. 2023, doi: 10.1016/j.solmat.2022.112091.

[64] T. Taskesen *et al.*, 'Steep sulfur gradient in CZTSSe solar cells by H2S-assisted rapid surface sulfurization', *RSC Adv*, vol. 11, no. 21, pp. 12687–12695, Mar. 2021, doi: 10.1039/d1ra00494h.

[65] M. Grossberg, J. Krustok, J. Raudoja, K. Timmo, M. Altosaar, and T. Raadik, 'Photoluminescence and Raman study of Cu2ZnSn(Se xS1 - X)4 monograins for photovoltaic applications', in *Thin Solid Films*, Aug. 2011, pp. 7403–7406. doi: 10.1016/j.tsf.2010.12.099.

[66] M. Dimitrievska *et al.*, 'Vibrational and structural properties of Cu2ZnSn(SxSe1-x)4 (0 ≤ x ≤ 1) solid solutions', in *2014 IEEE 40th Photovoltaic Specialist Conference, PVSC 2014*, Institute of Electrical and Electronics Engineers Inc., Oct. 2014, pp. 33–36. doi: 10.1109/PVSC.2014.6925064.

[67]   'Function Models', 2021. https://fityk.nieto.pl/model.html#function-types-and-functions (accessed Apr. 13, 2023).

[68]   M. Dimitrievska *et al.*, 'Multiwavelength excitation Raman scattering of Cu2ZnSn(SxSe1-x)4 (0 ≤ × ≤ 1) polycrystalline thin films: Vibrational properties of sulfoselenide solid solutions', *Appl Phys Lett*, vol. 105, no. 3, Jul. 2014, doi: 10.1063/1.4891333.

[69]   M. Dimitrievska, A. Fairbrother, E. Saucedo, A. Pérez-Rodríguez, and V. Izquierdo-Roca, 'Secondary phase and Cu substitutional defect dynamics in kesterite solar cells: Impact on optoelectronic properties', *Solar Energy Materials and Solar Cells*, vol. 149, pp. 304–309, May 2016, doi: 10.1016/j.solmat.2016.01.029.

[70]   H. Xie *et al.*, 'Impact of Sn(S,Se) secondary phases in Cu2ZnSn(S,Se)4 solar cells: A chemical route for their selective removal and absorber surface passivation', *ACS Appl Mater Interfaces*, vol. 6, no. 15, pp. 12744–12751, Aug. 2014, doi: 10.1021/am502609c.

[71]   T. S. Shyju, S. Anandhi, R. Suriakarthick, R. Gopalakrishnan, and P. Kuppusami, 'Mechanosynthesis, deposition and characterization of CZTS and CZTSe materials for solar cell applications', *J Solid State Chem*, vol. 227, pp. 165–177, Jul. 2015, doi: 10.1016/j.jssc.2015.03.033.

[72]   M. Dimitrievska, A. Fairbrother, A. Pérez-Rodríguez, E. Saucedo, and V. Izquierdo-Roca, 'Raman scattering crystalline assessment of polycrystalline Cu 2ZnSnS4 thin films for sustainable photovoltaic technologies: Phonon confinement model', *Acta Mater*, vol. 70, pp. 272–280, May 2014, doi: 10.1016/j.actamat.2014.02.035.

[73]   Kentaro Ito, *Copper Zinc Tin Sulfide-Based Thin-Film Solar Cells*. 2015.

[74]   M. Grossberg, O. Volobujeva, A. Penežko, R. Kaupmees, T. Raadik, and J. Krustok, 'Origin of photoluminescence from antimony selenide', *J Alloys Compd*, vol. 817, Mar. 2020, doi: 10.1016/j.jallcom.2019.152716.

[75]   K. Kneipp, H. Kneipp, I. Itzkan, R. R. Dasari, and M. S. Feld, 'Surface-enhanced non-linear Raman scattering at the single-molecule level', 1999. [Online]. Available: www.elsevier.nlrlocaterchemphys

[76]   A. P. Levanyuk and V. V Osipov, 'Edge luminescence of direct-gap semiconductors', 1981. [Online]. Available: http://iopscience.iop.org/0038-5670/24/3/R02

[77]   U. Saha and M. K. Alam, 'Boosting the efficiency of single junction kesterite solar cell using Ag mixed Cu2ZnSnS4 active layer†', *RSC Adv*, vol. 8, no. 9, pp. 4905–4913, 2018, doi: 10.1039/c7ra12352c.

[78]   M. V. Yakushev *et al.*, 'Radiative recombination in Cu2ZnSnSe4 thin films with Cu deficiency and Zn excess', *J Phys D Appl Phys*, vol. 48, no. 47, Nov. 2015, doi: 10.1088/0022-3727/48/47/475109.

[79]   M. Lang *et al.*, 'Luminescence properties of Cu2ZnSn(S,Se)4 solar cell absorbers: State filling versus screening of electrostatic potential fluctuations', *Phys Rev B*, vol. 95, no. 15, Apr. 2017, doi: 10.1103/PhysRevB.95.155202.

[80]   J. Krustok, H. Collan, M. Yakushev3, and K. Hjelt2, 'The Role of Spatial Potential Fluctuations in the Shape of the PL Bands of Multinary Semiconductor Compounds', 1999.

[81]   J. Krustok, J. Raudoja, M. Yakushev, R. D. Pilkington, and H. Collan, 'On the Shape of the Close-to-Band-Edge Photoluminescent Emission Spectrum in Compensated CuGaSe 2', 1999.

[82]   I. Dirnstorfer,) D M Hofmann, D. Meister, B. K. Meyer, W. Riedl, and F. Karg, 'Postgrowth thermal treatment of CuIn"Ga…Se 2 : Characterization of doping levels in In-rich thin films',

1999. [Online]. Available: http://pubs.aip.org/aip/jap/article-pdf/85/3/1423/10596898/1423_1_online.pdf

[83] M. Grossberg, P. Salu, J. Raudoja, and J. Krustok, 'Microphotoluminescence study of Cu 2 ZnSnS 4 polycrystals', 2013.

[84] M. V. Yakushev *et al.*, 'Influence of the copper content on the optical properties of CZTSe thin films', *Solar Energy Materials and Solar Cells*, vol. 168, pp. 69–77, Aug. 2017, doi: 10.1016/j.solmat.2017.04.022.

[85] S. Oueslati *et al.*, 'Effect of germanium incorporation on the properties of kesterite Cu2ZnSn(S,Se)4 monograins', *Thin Solid Films*, vol. 669, pp. 315–320, Jan. 2019, doi: 10.1016/j.tsf.2018.11.020.

[86] J. Krustok *et al.*, 'Observation of band gap fluctuations and carrier localization in Cu2CdGeSe4', *J Phys D Appl Phys*, vol. 52, no. 28, May 2019, doi: 10.1088/1361-6463/ab1afd.

[87] A. Jagomägi, J. Krustok, J. Raudoja, M. Grossberg, and M. Danilson, 'Deep and edge photoluminescence emission of CuInTe2', *Phys Status Solidi B Basic Res*, vol. 237, no. 2, Jun. 2003, doi: 10.1002/pssb.200301824.

[88] J. Márquez-Prieto *et al.*, 'Impact of the selenisation temperature on the structural and optical properties of CZTSe absorbers', *Solar Energy Materials and Solar Cells*, vol. 152, pp. 42–50, Aug. 2016, doi: 10.1016/j.solmat.2016.03.018.

[89] S. Siebentritt, N. Papathanasiou, and M. C. Lux-Steiner, 'Potential fluctuations in compensated chalcopyrites', in *Physica B: Condensed Matter*, Apr. 2006, pp. 831–833. doi: 10.1016/j.physb.2005.12.208.

[90] 'Ubrach tails'.

[91] J. Ri Krustok, H. Collan, and K. Hjelt, 'Does the low-temperature Arrhenius plot of the photoluminescence intensity in CdTe point towards an erroneous activation energy?', 1997.

[92] C. Kittel, *Introduction to Solid State Physics Charles Kittel*. 2005.

[93] J. Krustok *et al.*, 'Local strain-induced band gap fluctuations and exciton localization in aged WS2 monolayers', *AIP Adv*, vol. 7, no. 6, Jun. 2017, doi: 10.1063/1.4985299.

[94] Q. Li, S. J. Xu, M. H. Xie, and S. Y. Tong, 'A model for steady-state luminescence of localized-state ensemble', *Europhys Lett*, vol. 71, no. 6, pp. 994–1000, Sep. 2005, doi: 10.1209/epl/i2005-10170-7.

[95] J. Lee, E. S. Koteles, and M. O. Vassell, 'Luminescence linewidths of excitons in GaAs quantum wells below 150 K', 1986.

[96] 'Phonon', 2023. https://en.wikipedia.org/wiki/Phonon (accessed May 03, 2023).

[97] H. Esmaielpour *et al.*, 'Effect of occupation of the excited states and phonon broadening on the determination of the hot carrier temperature from continuous wave photoluminescence in InGaAsP quantum well absorbers', *Progress in Photovoltaics: Research and Applications*, vol. 25, no. 9, pp. 782–790, Sep. 2017, doi: 10.1002/pip.2890.

[98] G. Conibeer *et al.*, 'Hot Carrier Solar Cells: Materials with Modulated Phonon Energy for Slowed Carrier Cooling', 2013.

[99] Y. Rosenwaks, M. C. Hanna, D. H. Levi, D. M. Szmyd, R. K. Ahrenkiel, and A. J. Nozik, 'Hot-carrier cooling in GaAs: Quantum wells versus bulk', *Phys Rev B*, vol. 48, pp. 15–1993, 1993.

[100] C. J. Hages *et al.*, 'Identifying the Real Minority Carrier Lifetime in Nonideal Semiconductors: A Case Study of Kesterite Materials', *Adv Energy Mater*, vol. 7, no. 18, Sep. 2017, doi: 10.1002/aenm.201700167.

[101] T. H. Cheng, P. S. Kuo, C. Y. Ko, C. Y. Chen, and C. W. Liu, 'Electroluminescence from monocrystalline silicon solar cell', *J Appl Phys*, vol. 105, no. 10, 2009, doi: 10.1063/1.3117523.

[102] H. Herman, *Treatise on materials science and technology*. Academic Press, 1972.

[103] W. Siiocklev and A. W. T. Read, 'A SOLUBLE PROBLEM IN ENERGY HANDS Statistics of the Recombinations of Holes and Electrons', 1952.

[104] J. Wheatley and D. Halliday, 'I,OOO-IOO LIFETIME IN 8 ~ em N-TYPE QERMANIUM THEORETICAL CURVE FITTED TO', 1949.

[105] J. Krustok, R. Kaupmees, N. Abbasi, K. Muska, I. Mengü, and K. Timmo, 'Bandgap Fluctuations, Hot Carriers, and Band-to-Acceptor Recombination in Cu2ZnSn(S,Se)4 Microcrystals', *Physica Status Solidi - Rapid Research Letters*, 2023, doi: 10.1002/pssr.202300077.

[106] B. G. Mendis *et al.*, 'Nanometre-scale optical property fluctuations in Cu2ZnSnS4 revealed by low temperature cathodoluminescence', *Solar Energy Materials and Solar Cells*, vol. 174, pp. 65–76, Jan. 2018, doi: 10.1016/J.SOLMAT.2017.08.028.

APPENDIX

Check for updates

Bandgap Fluctuations, Hot Carriers, and Band-to-Acceptor Recombination in Cu₂ZnSn(S,Se)₄ Microcrystals

Jüri Krustok,* Reelika Kaupmees, Nafiseh Abbasi, Katri Muska, Idil Mengü, and Kristi Timmo

Temperature and laser power dependencies of the band-to-acceptor recombination in $Cu_2ZnSn(S_xSe_{1-x})_4$ ($x = 0.7$) microcrystals, which exhibit large bandgap energy fluctuations, are studied. The average depth of these fluctuations is approximately 79 meV. The shape of the corresponding wide photoluminescence (PL) band is analyzed using a modified localized-state ensemble model. The temperature dependence of this PL band is demonstrated to be influenced by the redistribution of holes between potential wells in the valence band with varying depths. The shape of this band at different temperatures is well fitted when an effective carrier temperature is introduced. This temperature is found to be approximately 300 K higher than the lattice temperature in the samples, and it is mainly caused by the very short minority carrier lifetime. According to the laser power-dependent PL studies, there is a consistent reduction in the effective carrier temperature as the laser power increases. This phenomenon is explained by the dominance of nonradiative Shockley–Read–Hall recombination at lower temperatures.

1. Introduction

Although it has been an active area of research for over half a century, the development of new materials for solar energy harvesting is currently a major focus in the renewable energy field. Kesterite $Cu_2ZnSn(S,Se)_4$ (CZTSSe) materials have emerged as a promising contender for widespread photovoltaic deployment in the future. These materials are made from nontoxic, earth-abundant components. Furthermore, they have excellent optoelectronic properties, making them highly suitable for achieving high power conversion efficiency.[1] Despite the increasing amount of research, the open-circuit voltage (V_{OC}) characteristics of the top-performing kesterite solar cells only reach 60% of the maximum value possible.[2] The primary causes for this significant deficit in V_{OC} are believed to be carrier recombination in the bulk and a high recombination rate at the interface between the absorber and buffer layers. Further research is required to gain a better understanding of the recombination

mechanisms present in kesterite compounds. Photoluminescence (PL) spectroscopy is frequently utilized to identify various defects and recombination processes. PL properties of kesterite materials are usually determined by a high concentration of charged intrinsic point defects. These uncompensated point defects give rise to electrostatic potential fluctuations, and, as a result, new recombination channels appear. They are related to valence and conduction band tail states. Moreover, potential fluctuations are responsible for spreading out defect levels inside of bandgap. Therefore, we can expect band-to-band (BB), band-to-tail (BT), and band-to-acceptor (BI) recombinations in these materials. In kesterites the small effective mass of electrons ($m_e/m_0 = 0.18$) compared with the high effective mass of holes ($m_p/m_0 = 2$)[3] creates a situation, where electrons are typically not localized inside potential wells created by charged defects or bandgap fluctuations and the distribution of holes between localized valence band tail states determines properties of PL bands.[4] All these recombinations were studied by Levanyuk and Osipov.[4] Later, it was shown that BI, BT, and BB recombinations are present in chalcopyrites[5–7] and also in kesterites like $Cu_2ZnSn(S,Se)_4$.[8–11] The observed low-temperature wide PL bands have an asymmetrical shape; the peak position exhibits a rapid redshift with temperature having a minimum value at around $T = 100–200$ K. With increasing laser power, the peak position shows a blueshift in the range of 10–20 meV per decade. All of these characteristics are observable in chalcopyrites. However, kesterites demonstrate extra Gaussian bandgap energy fluctuations, which are caused by differences in the spatial degree of Cu–Zn ordering, localized clusters of defects, or variations in composition. It is known that CZTSSe crystallizes in the disordered kesterite structure, where the 2d Wyckoff positions of the (001) cationic planes are randomly occupied by Cu and Zn atoms. The so-called ordered–disordered transition in CZTS and in CZTSe happens at $T = 260\,°C$ and $T = 200\,°C$, respectively.[12] Low-temperature ordered phase can have about 100 meV higher bandgap energy than the high-temperature disordered phase.[13] Simultaneous presence of both phases results in a double PL band structure with abnormally wide full width at half maximum (FWHM) of an aggregate band.[14] The disordered phase with a lower bandgap energy inside the mostly ordered lattice can create potential wells also for electrons initializing additional

J. Krustok, R. Kaupmees, N. Abbasi, K. Muska, I. Mengü, K. Timmo
Department of Materials and Environmental Technology
Tallinn University of Technology
Ehitajate tee 5, 19086 Tallinn, Estonia
E-mail: juri.krustok@ttu.ee

The ORCID identification number(s) for the author(s) of this article can be found under https://doi.org/10.1002/pssr.202300077.

56

tail-to-acceptor (TI) and tail-to-tail (TT) recombinations. As it was mentioned before, various defect clusters are also responsible for bandgap fluctuations, and rather deep potential wells for both holes and electrons can be found in kesterites.[15–17] It is proposed that these defect clusters are the main source of the kesterite band tails and bandgap energy fluctuations.[18]

The most common PL band in kesterites is a BI band. The theoretical model for the BI band was first introduced by Levanyuk and Osipov.[4] Later this model was improved by Jagomägi et al.[19] Unfortunately, all these models fail to describe the shape and temperature dependence of the BI band in cases of strong bandgap fluctuations. In this study, we will perform a detailed analysis of BI recombination in CZTSSe crystals with strong bandgap fluctuations.

2. Result and Discussion

The temperature dependence of the PL band in our CZTSSe sample is presented in **Figure 1**a.

The low-energy (LE) side of the wide PL band shows a Gaussian shape and the peak position displays a visible redshift with increasing temperature. Moreover, the PL band at low temperature has an asymmetric shape with a steeper decline on the high-energy (HE) side. It was shown previously in many articles[6,20–22] that the LE side of these asymmetric PL bands at low temperatures is more or less determined by the density of states function $\rho(E)$ while the temperature-dependent distribution function $f(E)$ controls the shape of the HE side of the PL band. A Gaussian density of states function is typical

for defect-related emission (BI) and for BT emission usually exponential shape is detected.[23] The PL band integral intensity Φ decreases with temperature according to the simple exponential law[24]

$$\Phi(T) = \Phi_0/[1 + \alpha_1 T^{3/2} + \alpha_2 T^{3/2}\exp(-E_A/kT)] \quad (1)$$

where Φ is the integrated intensity of the PL band, α_1 and α_2 are the process rate parameters, and E_A is the thermal activation energy (see Figure 1b. The calculated thermal activation energy $E_A = 121 \pm 8$ meV indicates that quite deep acceptor defects are involved in PL emission. The most probable defect having an activation energy in this range is the Cu_{Zn} acceptor defect.[12] Hence, we expect BI type of recombination where the occupation of acceptor levels is determined by the localized holes inside potential wells created by bandgap and/or potential fluctuations and electrons can be considered as free. It should be mentioned that at suitable temperatures and deeper bandgap fluctuations, it is possible that also electrons can localize inside potential wells created at the edge of the conduction band. The distribution of holes between potential wells with different depths is mostly determined by the temperature. At very low temperatures, holes will typically occupy shallow wells and thus giving rise to the HE part of the BI band. Increasing temperature leads to redistribution holes from shallow wells into deeper ones, and the corresponding emission band will shift toward LE (see **Figure 2**).

At higher temperatures, the PL band starts to blueshift because all localized holes are liberated and we are dealing with capturing free holes from the valence band into acceptor defect
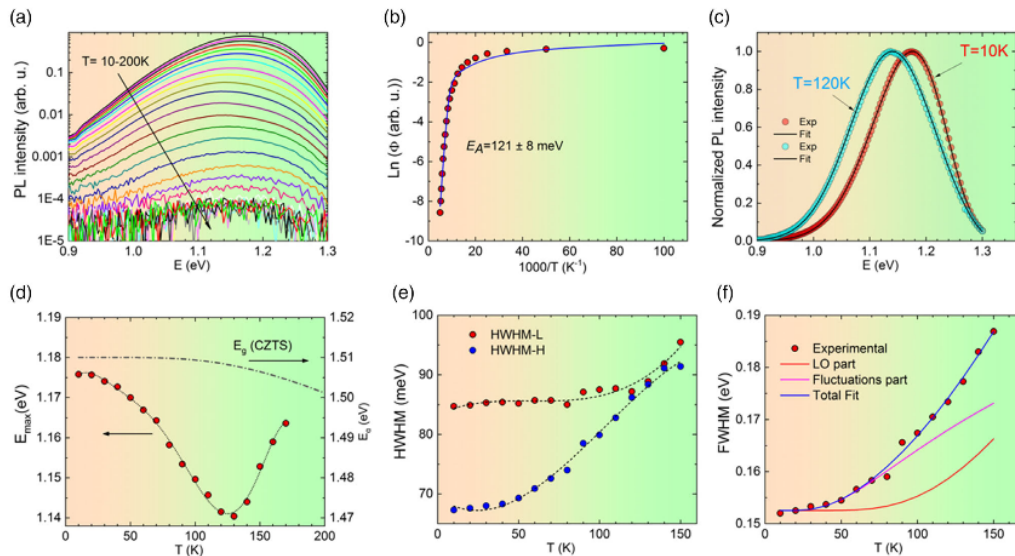
Figure 1. a) Temperature dependence of PL emission from CZTSSe microcrystals, b) thermal quenching of integral intensity Φ and fitting using Equation (1) (solid line), c) example of spectral fitting with Equation (2) for two different temperatures, d) temperature dependence of PL peak maximum E_{max} and bandgap energy of CZTS,[38] e) temperature dependence of HWHM values for low- and high-energy sides of the PL band, and f) temperature dependence of FWHM and result of fitting using Equation (3).

states. The distribution of holes between these localized states is affecting the shape and temperature dependence of the PL band. Similar situations were analyzed in different articles[20,25,26] by using the following simplified and modified localized-state ensemble (LSE) model

$$I(E) \propto \rho(E)f(E) \propto \exp\left[-\frac{(E-E_0)^2}{2\sigma^2}\right] * \frac{1}{\exp\left(\frac{E-E_a^*}{kT_e^*}\right) + \tau_{tr}/\tau_r} \quad (2)$$

where E_0 is a peak position and σ is the standard deviation of the distribution function of acceptor states, E_a^* is a "marking" level below which all the localized states are occupied by carriers (analogously to a quasi-Fermi level), and T_e^* is an effective carrier temperature. It should be mentioned that in the original LSE model[26] proposed for quantum dots the lattice temperature T was implemented. However, in order to fit the experimentally measured PL band shape, the effective carrier temperature T_e^* must be used. Although, in principle, a carrier temperature could be extracted from the HE tail of the PL band, increasing the lattice temperature also results in phonon-related broadening of the PL spectra. Also, the role of bandgap fluctuations increases with the depth of these fluctuations. Therefore, the extracted carrier temperature from PL spectra is usually higher than the real carrier temperature, and the difference is bigger at higher temperatures. Accordingly, the term "effective carrier temperature" was used here. At $T = 10$ K, $\sigma = 79$ meV and this value can be considered as the average amplitude of fluctuations. The average depth of electrostatic potential fluctuations in CZTSSe usually does not exceed 50 meV[27] and therefore we expect that bandgap fluctuations are dominant in our sample. The term $1/\tau_r$ represents the rate of radiative recombination, while $1/\tau_{tr}$ is the attempt-to-escape rate of the localized carriers. An analysis of Equation (2) shows that the shape of the HE tail is mainly determined by T_e^* while E_a^* and τ_{tr}/τ_r control the expanse of the distribution (see Figure S4, Supporting Information). Examples of the fittings with Equation (2) for $T = 10$ K and $T = 120$ K spectra are given in Figure 1c. The peak position of the PL band E_{max} shows quite rapid redshift with temperature and reaches a minimum value at $T = 130$ K. At $T > 130$ K, the peak position value starts to

increase again (see Figure 1d. The rate of this redshift at low temperatures exceeds the rate of bandgap energy E_g dependence shown for CZTS in Figure 1d. We assume that the $E_g(T)$ dependence in our CZTSSe samples has quite similar rate.

The temperature dependence of the half width at half maximum for HE and LE sides (HWHM-H and HWHM-L) is given in Figure 1e. As expected, the HWHM-L shows only a very small increase because of temperature independent $\rho(E)$ function at low temperatures while the HWHM-H is rapidly growing with temperature because of electron–phonon interaction and variation of T_e^* value. At about $T = 120$ K, the PL band has a symmetrical Gaussian shape. We also investigated the temperature dependence of FWHM (see Figure 1f. The FWHM value shows an unusually rapid increase with temperature that is not typical for pure electron–phonon interaction, and therefore we expect bandgap fluctuations to also contribute through effective carrier temperature T_e^*. The origin of FWHM behavior as a function of temperature in this case can be determined based on a model first presented by Lee et al.,[28] The total linewidth of the PL spectrum is given by

$$\text{FWHM}(T) = W_0 + \frac{W_1}{\left[\exp\left(\frac{\hbar\omega_{LO}}{kT}\right) - 1\right]} + W_2\exp(-E_{fl}/kT) \quad (3)$$

where W_0 denotes the width at $T = 0$ K including also inhomogeneous broadening, the second term represents the interaction with optical phonons, $\hbar\omega_{LO}$ is the LO-phonon energy ($\hbar\omega_{LO} = 41$ meV for CZTS was used),[29] and the last term represents how much fluctuations in the system can expand the linewidth of the PL spectra. The E_{fl} can be thought of as the average depth of shallow potential wells, which, as temperature rises, will be emptied, increasing the significance of deeper wells and, consequently, widening the PL band by widening the energy distribution of potential wells with different depth. We skipped an interaction with acoustic phonons because it is usually very weak. The result of the fitting with both components is given in Figure 1f where LO-phonon energy was fixed during fitting. The value of $E_{fl} = 14.8$ meV. Very similar energy values were obtained in ref. [30] as well.

The concept of the effective carrier temperature indicates that, although the energy distribution of charge carriers can be described by the Fermi–Dirac distribution, the effective carrier temperature T_e^* is higher than the lattice temperature T. The different temperatures of the carriers and the lattice are a natural outcome of the relatively short photocarrier lifetime τ, i.e., $T_e^* \sim \tau^{-1}$.[31,32] If a minority carrier lifetime is very short, excited carriers with high temperatures will recombine before they can "cool down" to lattice temperature T as a result of carrier–phonon interaction and carrier–carrier scattering. It is known that in kesterite compounds, the actual lifetime of the photoexcited carriers is extremely small and does not exceed values of hundreds of picoseconds.[12,33] Therefore, we also expect quite high T_e^* values. The temperature dependence of T_e^* is given in **Figure 3**a. At low temperatures, the effective carrier temperature increases as

$$T_e^*(T) = T_0^* + a_1/[\exp(a_2/kT) - 1] \quad (4)$$

where T_0^*, a_1, and a_2 are the fitting parameters. The increase of T_e^* corresponds to a decrease of τ with temperature, and this

Figure 2. Recombination model for the BI band in CZTSSe microcrystals with strong bandgap energy fluctuations. Note that deeper potential wells for holes (and also for electrons) affect mostly the LE side of the PL band, while shallow wells contribute to the HE side. The redistribution of holes between potential wells causes both redshift and blueshift of the PL band with increasing temperature.

58

Figure 3. a) Temperature dependence of an effective carrier temperature T_e^* and fitting result with Equation (4); b) PL spectra measured at $T = 10$ K using different laser powers. PL peak position shows a blueshift of 15 meV per decade of laser power; c) laser power dependence of T_e^*.

behavior is typical for different recombinations. At $T = 110$ K, the T_e^* shows a rapid drop, indicating a change in the recombination process. Indeed, in this temperature region, all localized holes are liberated, and the capture of holes by acceptor levels will be different.

Figure 3b presents the laser power dependence of the PL spectrum of CZTSSe measured at $T = 10$ K. The peak position of the PL band shows a blueshift of 15 meV per decade of laser power. This blueshift is quite typical for semiconductor materials with potential and/or bandgap fluctuations. The blueshift in our case can be attributed to the band filling effect and/or effect of decreasing of T_e^* with laser power. Indeed, Figure 3c shows a constant decease of T_e^* corresponding to an increase of carrier lifetime τ with increasing laser power. It is known that different types of nonradiative and radiative recombinations have also a different carrier lifetime dependence on laser power (see, e.g., ref. [34]) Usually, the effective minority carrier lifetime is determined by a combination of recombination rates

$$\frac{1}{\tau} = \frac{1}{\tau_{rad}} + \frac{1}{\tau_{Aug}} + \frac{1}{\tau_{SRH}} \tag{5}$$

where τ_{rad} is a radiative recombination lifetime, τ_{Aug} is a lifetime related to Auger recombination, and τ_{SRH} is a defect-related Shockley–Read–Hall (SRH) recombination lifetime. The SRH recombination was studied in a classical work[35] and it was shown that the minority carrier lifetime caused by SRH recombination increases in certain conditions with excess carrier concentration, i.e., with increasing laser power. For other recombinations, the lifetime usually decreases with laser power.[34] Consequently, the decrease of T_e^* with laser power is related to nonradiative SRH recombination dominating at low temperatures.

3. Conclusion

In conclusion, we conducted a PL study on CZTSSe microcrystals with large bandgap energy fluctuations in the temperature range of 10–200 K. We demonstrated that the PL band arises from band-to-acceptor recombination, and the depth of the acceptor defect was determined to be 121 meV. The shape and temperature dependence of this PL band were analyzed using a modified localized-state ensemble model, which employed

an effective carrier temperature T_e^* in place of the lattice temperature T. Our analysis showed that T_e^* rapidly decreased at $T = 110$ K, indicating a transformation in the recombination process. Furthermore, it was noted that there was a decrease in T_e^* as the laser power increased, which was linked to the prevalence of nonradiative SRH recombination at low temperatures.

4. Experimental Section

The CZTSSe microcrystals used in this study were synthesized by the molten salt (flux material) synthesis-growth method. As precursors, Cu powder (99.999%, Alfa Aesar), Sn shots (99.999%, Alfa Aesar), ZnS powder (99.999%, Alfa Aesar), S pieces (99.999%, Alfa Aesar), and Se shots (99.999%, Alfa Aesar) were used. As flux material, water-soluble potassium iodide with the mass ratio of liquid KI to solid CZTSSe of 1.2:1 (g/g) was used. The precursors with the intended initial composition of $Cu_{1.914}Zn_{1.08}Sn_{0.982}S_{2.68}Se_{1.32}$ and KI were weighed in desired amounts and ratios, loaded into a quartz ampoule, and mixed by shaking. The filled ampoule was degassed under a dynamic vacuum, sealed, and heated isothermally at 740 °C for 110 h. After cooling the ampoule to room temperature, the flux material was removed from the batch by leaching and rinsing with distilled water. The released microcrystal powder was dried in a hot-air oven at 50 °C and sieved into several narrow granulometric fractions between 38 and 125 μm. More details about the growth process of kesterite-based microcrystal powder can be found in ref. [36]. After synthesis, the powder was etched with 0.1 vol% Br in methanol for 60 s and with 10 wt% KCN aqueous solution for 90 s at room temperature, and afterward annealed isothermally in a vacuumed ampoule (volume ≈ 2 cm^3) at 740 °C 35 min. Then, the furnace was switched off until the ampoule reached room temperature. The composition of the main constituent elements in the CZTSSe powder crystals was analyzed by energy-dispersive X-ray spectroscopy (EDX) on HR-SEM Zeiss Merlin equipped with Bruker EDX-XFlash6/30 detector with an accelerating voltage of 20 kV. According to the EDX analysis, the postannealed CZTSSe crystals had an average composition of $Cu_{1.95}Zn_{1.03}Sn_{1.04}S_{2.81}Se_{1.19}$. Composition $[S]/([S] + [Se]) = 0.7$ was used to reduce the bandgap energy for a better match with solar spectrum. The room temperature bandgap energy for this composition is estimated to be near 1.4 eV.[37] The average size of used CZTSSe microcrystals was about 63–75 μm (see Figure S1, Supporting Information). The elemental composition of different crystals showed small fluctuations (see Figure S2, Supporting Information). Phase purity of CZTSSe powder crystals was verified by micro-Raman spectroscopy using Horiba's LabRam HR 800 spectrometer equipped with a cooled multichannel CCD detector in the backscattering configuration and a 532 nm laser line. Raman spectroscopy measurements verified the presence of the CZTSSe phase (see Figure S3, Supporting Information); no other phases were detected.

A 0.64 m focal length single grating (600 mm^{-1}) monochromator and the 442 nm line of a He–Cd laser with different powers were used for PL measurements. For PL signal detection, a Hamamatsu InGaAs photomultiplier tube (PMT) was used. A closed-cycle helium cryostat (Janis CCS-150) was employed to measure temperature dependencies of the PL spectra at temperatures from 10 to 200 K. More than 100 microcrystals were excited during the PL measurements using a laser spot with a diameter of 700 μm (maximum power density was 9 W cm^{-2}).

Conflict of Interest

The authors declare no conflict of interest.

Data Availability Statement

The data that support the findings of this study are available in the supplementary material of this article.

[1] A. Wang, M. He, M. A. Green, K. Sun, X. Hao, *Adv. Energy Mater.* **2023**, *13*, 2203046.
[2] S. Giraldo, Z. Jehl, M. Placidi, V. Izquierdo-Roca, A. Pérez-Rodríguez, E. Saucedo, *Adv. Mater.* **2019**, *31*, 1806692.
[3] U. Saha, M. K. Alam, *RSC Adv.* **2018**, *8*, 4905.
[4] A. P. Levanyuk, V. V. Osipov, *Sov. Phys. Usp.* **1981**, *24*, 187.
[5] J. Krustok, H. Collan, M. Yakushev, K. Hjelt, *Phys. Scr.* **1999**, *T79*, 179.
[6] J. Krustok, J. Raudoja, M. Yakushev, R. D. Pilkington, H. Collan, *Phys. Status Solidi* **1999**, *173*, 483.
[7] I. Dirnstorfer, M. Wagner, D. M. Hofmann, M. D. Lampert, F. Karg, B. K. Meyer, *Phys. Status Solidi A* **1998**, *168*, 163.
[8] M. Grossberg, P. Salu, J. Raudoja, J. Krustok, *J. Photonics Energy* **2013**, *3*, 030599.
[9] M. V. Yakushev, J. Márquez-Prieto, I. Forbes, P. R. Edwards, V. D. Zhivulko, A. V. Mudryi, J. Krustok, R. W. Martin, *J. Phys. D. Appl. Phys.* **2015**, *48*, 475109.
[10] M. V. Yakushev, M. A. Sulimov, J. Márquez-Prieto, I. Forbes, J. Krustok, P. R. Edwards, V. D. Zhivulko, O. M. Borodavchenko, A. V. Mudryi, R. W. Martin, *Sol. Energy Mater. Sol. Cells* **2017**, *168*, 69.
[11] S. Oueslati, M. Grossberg, M. Kauk-Kuusik, V. Mikli, K. Ernits, D. Meissner, J. Krustok, *Thin Solid Films* **2019**, *669*, 315.
[12] M. Grossberg, J. Krustok, C. J. Hages, D. M. Bishop, O. Gunawan, R. Scheer, S. M. Lyam, H. Hempel, S. Levcenco, T. Unold, *J. Phys. Energy* **2019**, *1*, 044002.
[13] G. Rey, A. Redinger, J. Sendler, T. P. Weiss, M. Thevenin, M. Guennou, B. El Adib, S. Siebentritt, *Appl. Phys. Lett.* **2014**, *105*, 112106.
[14] M. Grossberg, J. Krustok, J. Raudoja, T. Raadik, *Appl. Phys. Lett.* **2012**, *101*, 102102.
[15] M. Grossberg, T. Raadik, J. Raudoja, J. Krustok, *Curr. Appl. Phys.* **2014**, *14*, 447.
[16] S. Chen, J.-H. Yang, X. G. Gong, A. Walsh, S.-H. Wei, *Phys. Rev. B* **2010**, *81*, 245204.
[17] S. Chen, L.-W. Wang, A. Walsh, X. G. Gong, S.-H. Wei, *Appl. Phys. Lett.* **2012**, *101*, 223901.
[18] G. Rey, G. Larramona, S. Bourdais, C. Choné, B. Delatouche, A. Jacob, G. Dennler, S. Siebentritt, *Sol. Energy Mater. Sol. Cells* **2018**, *179*, 142.
[19] A. Jagomägi, J. Krustok, J. Raudoja, M. Grossberg, M. Danilson, M. Yakushev, *Phys. B Condens. Matter* **2003**, *337*, 369.
[20] J. Krustok, T. Raadik, R. Kaupmees, M. Grossberg, M. Kauk-Kuusik, K. Timmo, A. Mere, *J. Phys. D. Appl. Phys.* **2019**, *52*, 285102.
[21] A. Jagomägi, J. Krustok, J. Raudoja, M. Grossberg, M. Danilson, *Phys. Status Solidi* **2003**, *237*, R3.
[22] J. Márquez-Prieto, M. V. Yakushev, I. Forbes, J. Krustok, P. R. Edwards, V. D. Zhivulko, O. M. Borodavchenko, A. V. Mudryi, M. Dimitrievska, V. Izquerdo-Roca, N. M. Pearsall, R. W. Martin, *Sol. Energy Mater. Sol. Cells* **2016**, *152*, 42.
[23] S. Siebentritt, N. Papathanasiou, M. C. Lux-Steiner, *Phys. B Condens. Matter* **2006**, *376–377*, 831.
[24] J. Krustok, H. Collan, K. Hjelt, *J. Appl. Phys.* **1997**, *81*, 1442.
[25] J. Krustok, R. Kaupmees, R. Jaaniso, V. Kiisk, I. Sildos, B. Li, Y. Gong, *AIP Adv.* **2017**, *7*, 065005.
[26] Q. Li, S. J. Xu, M. H. Xie, S. Y. Tong, *Europhys. Lett.* **2005**, *71*, 994.
[27] M. Grossberg, J. Krustok, J. Raudoja, K. Timmo, M. Altosaar, T. Raadik, *Thin Solid Films* **2011**, *519*, 7403.
[28] J. Lee, E. S. Koteles, M. O. Vassell, *Phys. Rev. B* **1986**, *33*, 5512.
[29] C. Persson, R. Chen, H. Zhao, M. Kumar, D. Huang, in *Copper Zinc Tin Sulfide-Based Thin Film Solar Cells*, John Wiley & Sons Ltd, Chichester, UK, **2015**, pp. 75–105.
[30] H. Esmaielpour, V. R. Whiteside, L. C. Hirst, J. G. Tischler, C. T. Ellis, M. P. Lumb, D. V. Forbes, R. J. Walters, I. R. Sellers, *Prog. Photovoltaics Res. Appl.* **2017**, *25*, 782.
[31] G. Conibeer, S. Shrestha, S. Huang, R. Patterson, H. Xia, Y. Feng, P. Zhang, N. Gupta, M. Tayebjee, S. Smyth, Y. Liao, Z. Zhang, S. Chung, S. Lin, P. Wang, X. Dai, in *Next Generation Technologies for Solar Energy Conversion V, Vol 9178* **2014**, p. 917802.
[32] Y. Rosenwaks, M. C. Hanna, D. H. Levi, D. M. Szmyd, R. K. Ahrenkiel, A. J. Nozik, *Phys. Rev. B* **1993**, *48*, 14675.
[33] C. J. Hages, A. Redinger, S. Levcenko, H. Hempel, M. J. Koeper, R. Agrawal, D. Greiner, C. A. Kaufmann, T. Unold, *Adv. Energy Mater.* **2017**, *7*, 1700167.
[34] T.-H. Cheng, P.-S. Kuo, C.-Y. Ko, C.-Y. Chen, C. W. Liu, *J. Appl. Phys.* **2009**, *105*, 106107.
[35] W. Shockley, W. T. Read, *Phys. Rev.* **1952**, *87*, 835.
[36] K. Timmo, M. Altosaar, M. Pilvet, V. Mikli, M. Grossberg, M. Danilson, T. Raadik, R. Josepson, J. Krustok, M. Kauk-Kuusik, *J. Mater. Chem. A* **2019**, *7*, 24281.
[37] J. He, L. Sun, S. Chen, Y. Chen, P. Yang, J. Chu, *J. Alloys Compd.* **2012**, *511*, 129.
[38] W. Li, K. Jiang, J. Zhang, X. Chen, Z. Hu, S. Chen, L. Sun, J. Chu, *Phys. Chem. Chem. Phys.* **2012**, *14*, 9936.

60